# Multiscale Modelling Made Simple — "NanoBridge" A Computational Platform for Next-Gen Simulations of Novel Devices Incorporating 2D Materials

The demand for electronics is exponentially increasing; electronic devices continue to shrink in size while at the same time are required to deliver better performance and expanding functionality. Furthermore, these devices also require exponentially more power to operate. Incorporating the use of novel 2D materials with unprecedented properties could provide a response to this challenge.

When numerically studying the performance of devices incorporating 2D materials, the primary hurdle lies in addressing the extreme geometrical aspect-ratio between nanostructured materials and device environments, the low dimensionality of the materials, and the coexistence of multi-physics phenomena involving electromagnetism (EM), charge propagation, heat transfer, amongst others. The use of this multi-physics (multiscale) toolkit provides high predictive capabilities and is a source of helpful information to manage and direct the design and manufacturing phase of the devices.

The computational platform offers simulation engines covering the entire range of atomic-scale simulation methods for the materials and subsequently devices of interest, which develops and integrates:

1. ab-initio simulations at atomistic level;
2. Monte Carlo simulations at meso-scale level;
3. full-wave simulations at continuum level.

The *in-silico* approaches included in the platform complement each other: for successful use of atomic to meso-scale modelling, it is essential to have easy access to all the methods to combine them. Many different developed software packages are focused on one or some calculation methods; for this reason the development of a massive computational platform based on different tools has required a large effort for compilation, installation, and learning the input/output syntax. The tools are not fully compatible with any other packages; then learning the additional syntax within the modelling class has required another large effort. Moreover, a single simulation tool method does not have all the required capabilities for the purposes of NanoBridge; hence, several different tools within each modelling class are needed to solve a given problem, and a significant effort has

been invested to master each of them. We have developed a computational tool based on different simulation engines, covering the entire range of atomic-scale simulation methods, then reaching full-wave simulations.

In detail, we will use atomistic modelling and simulations to provide information about chemical-physical phenomena and to obtain constitutive relations to be included in simulators at the continuum level, to refine the calculation and to achieve truthful and reliable results. This means that *the architecture of our computational platform is based on a bridge between the discrete and continuous levels* (**Figure 1**).

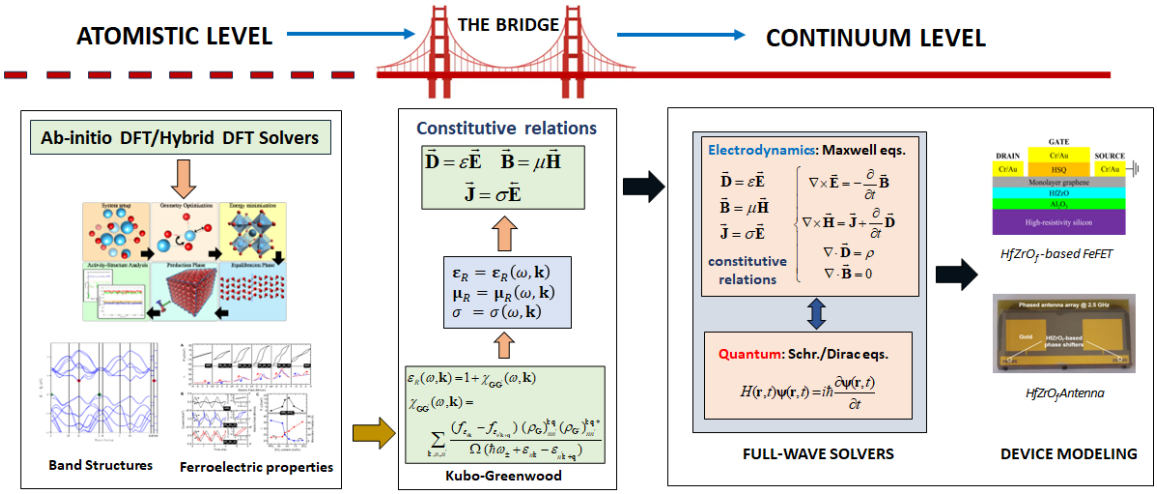


**Figure 1:** Description of NanoBridge Multiphysics platform. The different levels of theory are reported to highlight the connection point between discrete and continuum simulations.

At the atomistic level, the entire range of atomic-scale simulation methods is included, moving from near-exact quantum mechanical calculations to approximate simulations, and we will choose the best method to use in relation to the effect to investigate. The basic concept is that the in-silico approaches included in the platform complement each other: for successful use of atomic to meso-scale modelling, it is essential to have easy access to all the methods to combine them. For this reason, we use Density Functional Theory (DFT) as the most important first-principle computational method, including corrective terms if necessary, and compiling parameter files for semi-empirical calculations (**Figure 2**).

More in detail, Quantum Atomistic ToolKit (Q-ATK) [1] represents the most important software used inside the proposed computational platform. It is a released software with licenses that allows generating simulation models through its modern graphical user interface (GUI). It includes many different simulation methodologies required, and all the computationally demanding modules may be run in parallel on many processors at once, using message passing between processes and/or shared-memory threading and in a multi-level approach.

Another software adopted is Quantum Espresso (QE) [2], which is an integrated suite of Open-Source computer codes used inside the platform. The GPU-accelerated version of this suite is installed on High Performance Computing (HPC) Center at Cineca ISCRA platform in Casalecchio di Reno [3] (Bologna, Italy), and the acceleration is the most important advantage in the use of QE by remote way. Using the same input/output syntax, we have modelled atomistic systems and carried out computational methodologies

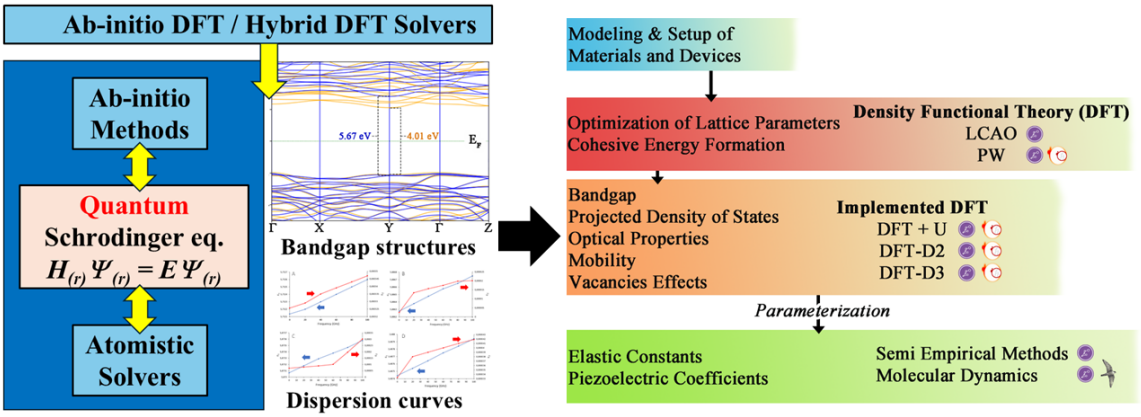


**Figure 2:** Description of the computational platform. The purple icon refers to the possible use of Quantum Atomistic ToolKit (Q-ATK) software, while the white and red symbol remarks the possibility to use QuantumEspresso (QE) package; the hawk icon highlights the possible use of GROMACS software.

using Q-ATK, then each input file has been accompanied by a command file to direct the simulation in QE. With the Q-ATK–QE linkage we have simultaneously conducted many different calculations leveraging both local computing resources and remote computing clusters.

Another part of our computational platform is represented by GROMACS, a versatile package [4] able to perform molecular dynamics (MD) simulations for systems with hundreds to millions of particles. This software is a free licensed package which includes many different force fields such as LAMMPS [5] and CLAYFF [6] that can be implemented with parameters obtained through other investigations based on other computational suites. Our approach is to use Q-ATK and QE to obtain precise parameterizations for materials of interest and then to simulate their properties using the force field (FF) and semi-empirical (SE) methods. Still concerning GROMACS, a GPU accelerated version is installed on HPC Cineca platform (*vide supra*), and we have performed highly extensive simulations obtaining results in a very reasonable time. The computational platform includes the most important FF packages implemented with empirical evidence but, more importantly, the predefined literature parameter sets can be invoked from the NanoLab GUI included in Q-ATK. It is also possible to specify custom FF parameters via the Potential Editor tool in a Python script from Q-ATK and QE to implement FFs included in GROMACS. This way, we have carried out fast simulations including a high number of atoms, decreasing the accuracy degree and maintaining high reliability thanks to the refined parameters.

In reference to the computational methods, the starting framework of our platform for *ab initio* electronic-structure theory is represented by DFT, which provides computationally tractable solutions to the electronic many-body problem and gives high predictive power with respect to experiments [7]. The exchange-correlation (xc) functional is the only formal approximation in the DFT approach, since the exact functional is unknown. Our

platform supports a large range of approximate xc functionals including the local density (LDA) and generalized gradient (GGA) approximations. Furthermore, the computational platform supports spin-unpolarized and spin-polarized (both collinear and noncollinear) variants for each xc functional. All DFT results are based on the use of GGA functionals [8] which assume that the exchange and correlation energy at a point depends not only on the density at that point, but also on its gradient of electron density following equation (1):

$$E_{xc}^{\mathrm{GGA}}[n] = \int n(\mathbf{r})\, \varepsilon_{xc}(n(\mathbf{r}),\, |\nabla n(\mathbf{r})|)\, d\mathbf{r} \tag{1}$$

in which the term $|\nabla n(\mathbf{r})|$ is the addition for the gradient, and the density $n(\mathbf{r})$ represents the number of electrons per unit volume.

In periodic systems a given element may be present in different spatial arrangements displaying vastly different physical and chemical properties; for this reason, an elemental basis set that is independent of physical properties of materials may lead to significant simulation inaccuracies. To avoid such a lack of material specificity within a given basis set, it is of crucial importance to choose between different basis sets to better represent the shapes of orbitals and then to simulate the correct wavefunction overlapping. For this purpose, inside our platform DFT is implemented with the linear combination of atomic orbitals (LCAO) and the plane-wave (PW) basis set approaches, and both are obviously combined with different pseudopotential methods.

DFT-LCAO can be used with Q-ATK software, and it represents an efficient implementation for layered materials, interface structures, models with vacancies and, in general, for systems with mixed boundary conditions [9]. For this formalism, the single-electron eigenfunctions $\psi_\alpha$ are expanded in a set of finite-range atomic-like basis functions $\varphi_i$ following equation (2):

$$\psi_\alpha(\mathbf{r}) = \sum_i c_{\alpha i}\, \varphi_i(\mathbf{r}) \tag{2}$$

The use of all-electron LCAO calculations allowed us to accurately describe the electronic distributions both in the valence and in the core region with a limited number of basis functions. The local nature of the basis allows treatment both of finite systems and of systems with periodic boundary conditions in one, two, or three dimensions.

On the other hand, the plane-wave (PW) representation implemented in the platform is ideally suited for bulk configurations with periodic boundary [10], and it can be used with Q-ATK and QE. In this case eigenfunctions are expanded in terms of PW basis functions following equation (3):

$$\psi_\alpha(\mathbf{r}) = \sum_{|\mathbf{g}|<g_{\max}} c_{\alpha,\mathbf{g}}\, e^{i\mathbf{g}\cdot\mathbf{r}} \tag{3}$$

where $\alpha$ denotes both the wave vector $\mathbf{k}$ and the band index $n$, and $\mathbf{g}$ are reciprocal lattice vectors. The upper threshold for the reciprocal lattice-vector lengths included in the PW expansion ($g_{\max}$) is determined by a kinetic-energy (wavefunction) cutoff energy $E_{\mathrm{cut}}$ with equation (4):

$$\frac{\hbar^2 g_{\max}^2}{2m} < E_{\mathrm{cut}} \tag{4}$$

PW methods are the most popular in periodic systems calculations. Plane waves are an orthonormal complete set, where any function belonging to the class of continuous formalizable functions can be expanded with arbitrary precision in such a basis set.

Since DFT is well known to reproduce the steady-state properties of materials in an accurate way, the purpose of the NanoBridge simulation approach is to investigate the excited state phenomena with the aim to predict the physical-chemical behaviour of the studied materials. Moreover, the inclusion of polyelectronic atoms such as Hf, Zr, Mo, and V leads to some important effects that must be considered in the simulations and that are not correctly described by canonical DFT approach. One example is the inclusion of the strong on-site Coulomb interactions of localized $d$ and $f$ electrons involved in the chemical bonds, as for Hf, Zr, and V. We have described these repulsive terms by adding a Hubbard corrective term to the DFT approach following equation (5); this approach has been extensively applied by the group to $HfO_2$ and $HfZrO_2$ high-$\kappa$ oxides relevant for MIM and gate-stack devices [11–13]:

$$E_U = \frac{1}{2} \sum_l U_l \left( n_l - n_l^2 \right) \tag{5}$$

where $n_l$ is the projection onto an atomic shell $l$, and $U_l$ is the Hubbard $U$ for that shell. The energy term $E_U$ is zero for a fully occupied or unoccupied shell, but positive for a fractionally occupied shell. This method is called DFT+U [14] and can be adopted with both LCAO and PW basis sets. For high-$\kappa$ gate oxides such as $HfO_2$ and $HfZrO_2$, the group has shown that the DFT+U correction is essential to correctly reproduce the bandgap and the dielectric response of all relevant polymorphs (monoclinic, orthorhombic, cubic), and to quantify the role of oxygen vacancies on transport [11–13, 15, 16]. Similar DFT+U analysis was applied to $VO_2$ polymorphs (monoclinic, metallic B phase) and their interfaces with perovskite substrates [17–19], and to SnSe/graphene heterostructures where a negative dielectric constant (plasmonic regime) was predicted in the 24–169 THz range [20].

Another important example of effects that need to be reproduced is represented by the van der Waals dispersions for layered materials, as for $MoS_2$, $WSe_2$ or graphene. In this case, both DFT-LCAO and DFT-PW methods can be implemented with two-body and three-body dispersion corrections by Grimme with approaches called DFT-D2 [21] and DFT-D3 [22], respectively. The group has systematically applied these corrections to 2D semiconductors and high-$\kappa$ oxides, building a body of work that spans graphene-based diodes [23], transition-metal dichalcogenides ($WSe_2$, SnSe/graphene heterostructures, Cu/$VSe_2$) [20, 24, 25], vanadium dioxide polymorphs [17–19], and hafnium-based oxides [11–13, 15]. For the first method, we have added a pair-wise atom-atom potential to the DFT approach following (6):

$$\frac{C_{6,ij}}{r_{ij,L}^6} \tag{6}$$

where $C_{6,ij}$ is the dispersion coefficient obtained by DFT calculations of polarizabilities and ionization potentials of the isolated atoms, while $r_{ij,L}^6$ is the distance between the atoms as a function of the translation in the unit cell $L$. Another dispersion correction method for density functionals is DFT-D3, which is a refined version of DFT-D2. The biggest difference with its predecessor is that its dispersion coefficients are fully flexible and system dependent. For this reason, the $C_6$ terms are no longer scaled, and the higher $C_n$ terms are necessary to adapt the potential specifically to the DFT approach adopted.

Since only the outermost electrons determine the formation of chemical bonds with other atoms, with the aim to approximate the effects of core electrons avoiding explicit DFT calculations of core electrons, our platform uses pseudopotentials (PPs) and currently

supports both scalar-relativistic and fully relativistic norm-conserving PPs [26]. The computational platform is shipped with built-in databases of well-tested PPs covering all elements up to $Z = 83$ (Bi) and excluding lanthanides. The most useful PPs for our simulations are SG15 [27] and PseudoDojo [28] sets. These are two modern norm-conserving PP types with multiple projectors for each angular momentum, to ensure high accuracy. Both sets contain scalar-relativistic and fully relativistic PPs for each element.

Since the calculation of some properties of interest for the project require the inclusion of many atoms (e.g., for the mechanical properties of materials), other important approaches considered in the proposed computational platform are semiempirical (SE) methods and molecular dynamics simulations based on the FF approach. The use of computationally fast alternatives to DFT such as SE methods is related to the use of libraries with precalculated parameters. Our multi-software platform allowed us to generate specific packages to include in the SE calculation, avoiding self-consistent loops. In detail, transport calculations for obtaining $I$–$V$ characteristic curves and transmission pathways plots were all based on SE Tight-Binding (TB) approach [29] and Non-Equilibrium Green's Function (NEGF) formalism [30]. The group has applied this methodology to: geometric graphene self-switching diodes using SCC-DFTB [23, 31]; $HfO_2$- and $HfZrO_2$-based MIM diodes using DFT+NEGF [15, 16, 32]; TMD heterostructures and SnSe/graphene interfaces [20, 24, 33]; and graphene plasmonic emission at THz frequencies [34, 35]. This method treats the effect of the external potential on the entire system (atomic and trench regions) with desirable computational efficiency and with quantitative agreement with experimental results as reported in the result section.

On the other hand, the FF approach is fully integrated in the Python framework, and then, as for the SE methods, the FF parameters can be implemented with DFT-derived parameters. The FF approach has allowed us to carry out MD simulations using empirical potential models. The simulation engine also allows assigning different FFs to different sub-systems. The empirical potential for each sub-system and the interactions between them can be customized as desired using Python scripting. Our computational platform currently includes more than 300 predefined literature parameter sets, which can conveniently be invoked from the GUI and can be implemented using the approach that has been previously described for the SE implementation.

## From DFT to Semiempirical Methods: a Hierarchical Strategy for Metal–Dielectric Interfaces

A key challenge in modelling real devices – such as Metal-Insulator-Metal (MIM) diodes or high-$\kappa$ gate stacks – is the coexistence of very different length scales: the electronic structure of the metal–oxide interface is intrinsically quantum mechanical and must be described at the *ab initio* level, yet the actual contact regions in fabricated devices extend over tens to hundreds of nanometres, a size range that makes full DFT completely intractable. Our platform addresses this challenge through a *hierarchical, DFT-seeded semiempirical strategy* consisting of three successive steps described below and summarised in Figure 2.

**Step 1 – DFT reference calculations for the interface.** The starting point is a well-converged DFT calculation of a representative supercell of the metal–dielectric interface (e.g., Ti/$HfO_2$, TiN/$Al_2O_3$, or Au/$MoS_2$). Using GGA functionals augmented

with DFT-D3 dispersion corrections and, when necessary, DFT+U corrections for the localised $d$-orbitals of the metal or the oxygen $p$-states of the oxide [36,37], we extract the following quantities:

- band alignment and Schottky barrier height at the interface;
- charge density redistribution and induced dipole layer;
- optimised geometry (bond lengths, rumpling, relaxation depth);
- on-site energies and transfer integrals for the interfacial atom pairs.

This DFT reference calculation is computationally expensive (typically hundreds of atoms, several hundred CPU-hours on HPC) but is run *only once* per interface type. Its output directly parametrises the lower-level models described below.

**Step 2 – DFTB / Slater–Koster tight-binding for the extended contact region.** Once the DFT reference is available, we map the Kohn–Sham Hamiltonian onto a *Density Functional Tight-Binding* (DFTB) model [38–40]. In DFTB, the total energy is written as:

$$E_{\mathrm{DFTB}} = \sum_i n_i \langle \psi_i | \hat{H}^0 | \psi_i \rangle + \frac{1}{2} \sum_{\alpha\beta} \gamma_{\alpha\beta}\, \Delta q_\alpha \Delta q_\beta + E_{\mathrm{rep}} \tag{7}$$

where $\hat{H}^0$ is the zeroth-order Hamiltonian constructed from DFT-calculated atomic potentials, $\gamma_{\alpha\beta}$ is a two-centre Coulomb kernel that accounts for charge-transfer (second-order, SCC-DFTB [38]), $\Delta q_\alpha$ are Mulliken charge fluctuations, and $E_{\mathrm{rep}}$ is a short-range repulsive pair potential fitted to DFT energy–distance curves [41].

The Hamiltonian and overlap matrix elements are expressed through the **Slater–Koster** (SK) two-centre integrals [42]:

$$H_{\mu\nu}(\mathbf{R}) = \sum_m V_{\ell_\mu \ell_\nu m}(|\mathbf{R}|)\; D^{(\ell_\mu)}_{\mu m}(\hat{\mathbf{R}})\; D^{(\ell_\nu)}_{\nu m}(\hat{\mathbf{R}}) \tag{8}$$

where $V_{\ell_\mu \ell_\nu m}(R)$ are the SK bond integrals (tabulated as spline functions of interatomic distance $R$), and $D^{(\ell)}$ are rotation matrices that decompose the $\sigma$, $\pi$, $\delta$ contributions for each orbital pair $(\ell_\mu, \ell_\nu)$. The SK tables are extracted directly from our DFT calculations (Step 1) using the LCAO Hamiltonian of Q-ATK, ensuring that the DFTB model is *material-specific* rather than generic.

The SCC-DFTB method, as implemented in DFTB+ [43] and Q-ATK, scales as $\mathcal{O}(N^2)$–$\mathcal{O}(N^3)$ with system size $N$ but is typically $10^2$–$10^3$ times faster than full DFT for equivalent system sizes (see Figure 3), making it the method of choice for contact regions containing $10^2$–$10^4$ atoms. The group has applied SCC-DFTB+NEGF to geometric graphene diodes with sub-10 nm necks [23], achieving quantitative agreement with available experimental $I$–$V$ data for all three neck sizes studied. Transport $I$–$V$ curves are then obtained by coupling DFTB with the NEGF formalism [30,44], retaining the full quantum coherence of the Landauer–Büttiker framework (equations 10–14).

**Step 3 – Extended Hückel Theory for large-scale contact geometries.** When the geometrical dimensions of the metal–dielectric contacts become large – typically above several tens of nanometres lateral size, or when modelling entire via structures, interconnects, or multi-layer stacks – even DFTB becomes computationally prohibitive. In these

regimes, our platform falls back on the **Extended Hückel Theory** (EHT) [45, 46], the simplest semiempirical tight-binding approach. In EHT, the Hamiltonian matrix elements are approximated as:

$$H_{\mu\nu} = \frac{K}{2}\left(H_{\mu\mu} + H_{\nu\nu}\right) S_{\mu\nu} \tag{9}$$

where $H_{\mu\mu}$, $H_{\nu\nu}$ are the valence-state ionization energies (VSIEs) of the respective atomic orbitals $\mu$, $\nu$ (taken from Slater-type orbital (STO) tables fitted to atomic DFT calculations), $S_{\mu\nu}$ is the overlap integral computed analytically from STO exponents, and $K \approx 1.75$ is the Wolfsberg–Helmholtz constant [45].

Although EHT neglects self-consistency, the parametric freedom provided by the VSIEs and the STO exponents – when calibrated against the DFT reference of Step 1 – yields a model that correctly reproduces:

- the orbital symmetry and nodal structure of the relevant frontier states;
- the qualitative band alignment across the interface;
- transmission functions and $I$–$V$ characteristics in the low-bias linear regime [44, 46].

The key advantage of EHT is its extreme computational speed: the Hamiltonian is built in a single non-self-consistent pass ($\mathcal{O}(N)$ matrix fill, $\mathcal{O}(N^3)$ diagonalisation), allowing device geometries with $10^4$–$10^6$ atoms to be treated with NEGF transport on a single workstation. This makes EHT the natural bridge between the atomistic world and continuum drift-diffusion models (Figure 1). Another advantage in the use of EHT is the possibility to use different parameter sets, such as Hoffman, Muller, and Cedra packages, already implemented in Q-ATK. The possibility of choosing between different sets of parameters allows for efficient calibration of the method in relation to the type of interfaces and the size of the device, allowing for modulation between the degree of accuracy and computational costs. Hoffmann Parameters represent the original, foundational EHT set primarily targeting systems with $s$ and $p$ orbitals. Muller parameter set has been developed to describe $d$ orbitals systems, while Cedra parameters are a more modern adaptation focused on improving accuracy and transferability in extended systems, particularly for transition metals (*e.g.*, Pt) in surface or band structure calculations, employing more sophisticated atomic orbital representations. Together with the parameter set, EHT offers the possibility of discriminating between two different weighting schemes. In this perspective, the Wolfsberg-Helmholz ($WH$) approximation is the fundamental method used to calculate off-diagonal Hamiltonian matrix elements, while Roald Hoffmann ($RH$) popularized and standardized this approach by defining specific parameters, most notably the empirical constant $K$ described in eq 9.

**Workflow summary and applicability map.** Table 1 summarises the recommended method choice as a function of system size and required accuracy for the simulation of metal–dielectric contact regions.

It is important to stress that the three semiempirical tiers are not independent black boxes: they form a *connected chain* in which DFT provides the electronic-structure anchor, DFTB inherits the SK integrals and repulsive potentials from DFT, and EHT inherits the VSIEs and STO exponents from both DFT and DFTB. This self-consistent parametrisation cascade guarantees that even the most approximate EHT calculation retains material-specific accuracy for the property of interest – namely, the low-energy electronic structure

**Table 1:** Recommended simulation method as a function of system size and accuracy target for metal–dielectric interface transport calculations.

| Method | System size | Rel. cost | Best use case |
|---|---|---|---|
| DFT (GGA/+U/D3) | <500 atoms | reference | Interface geometry, band alignment, SK table generation |
| SCC-DFTB (SK) | $10^2$–$10^4$ atoms | $\times 10^{-3}$ | $I$–$V$ curves, NEGF transport of extended contacts |
| Extended Hückel | $10^4$–$10^6$ atoms | $\times 10^{-6}$ | Large-area contacts, interconnects, qualitative transport |
| Force Field (FF/MD) | $> 10^4$ atoms | $\times 10^{-8}$ | Structural relaxation, thermal effects, no electronic transport |

and transport characteristics of the metal–dielectric junction.

To give an idea about the computational cost of the different atomic-scale simulation methods included in our platform, the computational speed of the methods has been compared when simulating increasingly larger structures of $HfO_2$ (**Figure 3**).

The measure of speed is referred to the number of molecular dynamics steps that are feasible within 24 h when run in parallel on 16 computing cores. This comparison has been carried out on a 16-core central processing unit (CPU) of type Intel i9-10900K. The CPU times show that the PW approach is computationally demanding for higher systems, while the LCAO approach can be more than an order of magnitude faster for systems with more than 100 atoms.

Despite the high degree of accuracy achieved by using software in a combined way, materials can exhibit different chemical and physical properties depending on their specific dimensions and the circuit context in which they are located. Therefore, it is necessary to recreate the boundary conditions for each component in order to simulate an entire device. We now introduce the atomic-scale methodology used in simulated devices. All the simulations have been performed again with Q-ATK software, using SE method [29, 47] implemented by tight-binding (TB) calculations. From our knowledge, Q-ATK is the unique atomistic software with the capabilities of modelling the concept devices. Firstly, the modelling of devices such as Metal-Insulator-Metal (MIM), self-switching (SS) or geometric diodes must be performed using the previously optimized structures as single monolayers and discrete-sized systems, then the non-equilibrium Green's function (NEGF) will be used to calculate the self-consistent device potential and charge distribution [48, 49]. The multi-grid Poisson solver is the adopted approach to predict the Hartree energy by solving the Poisson equation. Meanwhile, the non-self-consistent part of the tight-binding Hamiltonian will be parametrized using the Slater–Koster model in which the distance-dependence of the matrix elements is given as a numerical function [29].

Once the self-consistent non-equilibrium density matrix will be obtained, the transport property and current amount of graphene devices have been calculated by using the

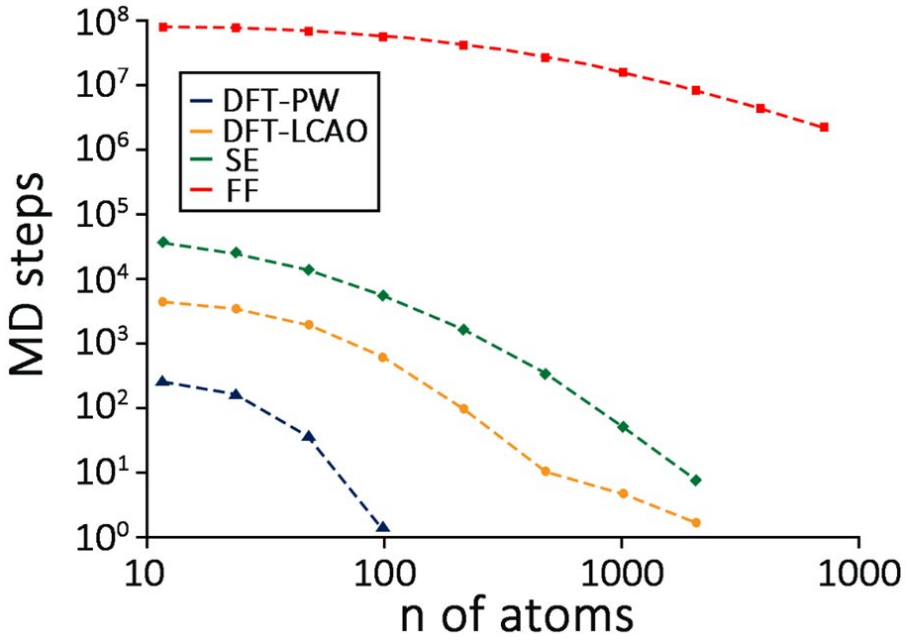


**Figure 3:** Comparison of the simulation methods available in our platform, considering the total number of molecular dynamics steps performed in 24 h (MD steps) against system size (number of atoms) of monoclinic $HfO_2$.

transmission coefficient $T$ at electron energy $E$ determined from the retarded Landauer formula [50]:

$$I(V_L, T_L, V_R, T_R) = \frac{e}{h} \sum_{\sigma} \int T_\sigma(E) \left[ f\left(\frac{E-\mu_R}{k_\beta T_R}\right) - f\left(\frac{E-\mu_L}{k_\beta T_L}\right) \right] dE \tag{10}$$

where $f$ is the Fermi function, $T_L/T_R$ are the electron temperatures of the left/right electrode, and $T_\sigma(E)$ is the transmission coefficient for the spin component $\sigma$. Meanwhile, the chemical potentials of the right/left electrode and $V_{\text{bias}}$ can be defined by equations (11)–(14):

$$\mu_R = E_F^R - eV_R \tag{11}$$

$$\mu_L = E_F^L - eV_L \tag{12}$$

$$\mu_R - \mu_L = eV_{\text{bias}} \tag{13}$$

$$V_{\text{bias}} = V_L - V_R \tag{14}$$

Beginning with the outcomes of the DFT simulations (e.g., band structure, charge wavefunctions, etc.), a rigorous process rooted in the Kubo–Greenwood formalism is utilized to incorporate the quantum properties of materials into electromagnetic (EM) constitutive relations [51]. This integration enables precise and rigorous EM simulations of complex devices. EM solvers, whether commercial or in-house, typically include databases containing information on all known materials. However, these databases inevitably lack the permittivity and permeability data for novel materials. Computing these parameters for novel materials presents a significant challenge and was among the most noteworthy scientific advancements of our computational platform [52].

## Electronic Structure and Band Alignment at Metal–Dielectric Interfaces

A critical prerequisite for any reliable transport simulation of MIM diodes (such as $Pt/ZrO_2/Ti$) or transistor-like devices is an accurate description of the electronic structure at the metal–dielectric interface. This includes the valence and conduction band positions relative to the metal Fermi level, the Schottky barrier height $\Phi_B$, and the depth of interface-induced gap states. In our platform, these quantities are computed from DFT supercell calculations using the *branch-point energy* (charge neutrality level) approach [36], combined with the macroscopic averaging technique [10] to align the electrostatic potential across the interface. The same methodology applies equally to metal/2D-material interfaces (e.g. $Au/MoS_2$, Ti/graphene) and to metal/high-$\kappa$ oxide stacks (e.g. $Pt/ZrO_2$, $Ti/HfO_2$).

Figure 4 illustrates the three key DFT outputs for a representative metal–dielectric heterostructure: (a) the electronic band structure of the 2D material (here $MoS_2$), showing the direct bandgap at the K point; (b) the projected density of states (PDOS) decomposed into metal and semiconductor contributions, which reveals hybridised interface states inside the gap; and (c) the band alignment diagram with the Schottky barrier $\Phi_B$ annotated. These results are used directly to set the on-site energies in the DFTB Hamiltonian and the VSIEs in the EHT model (Section above), ensuring consistency across all simulation tiers.

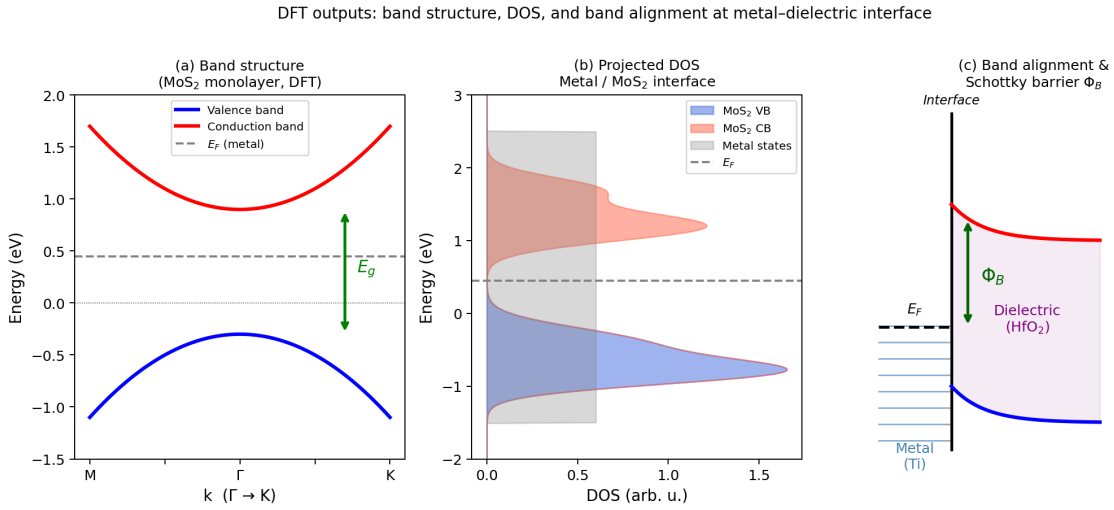


**Figure 4:** DFT-computed electronic properties at a representative metal–dielectric interface (generic example). (a) Band structure of a 2D semiconductor (e.g. $MoS_2$ monolayer) along the Γ–M–K path, showing the direct bandgap at K. (b) Projected DOS decomposed into metal and semiconductor contributions; interface-induced gap states appear inside the semiconductor gap. (c) Band alignment diagram with Schottky barrier height $\Phi_B$ annotated; the interface dipole $\Delta_{\text{dip}}$ shifts the barrier from the Schottky–Mott prediction. All results with GGA-PBE + DFT-D3 + norm-conserving pseudopotentials (Q-ATK or QE).

The Schottky barrier height is extracted as:

$$\Phi_B = \chi_s + \frac{E_g}{2} - \phi_m + \Delta_{\text{dip}} \tag{15}$$

where $\chi_s$ is the semiconductor electron affinity, $E_g$ the bandgap, $\phi_m$ the metal work function, and $\Delta_{\text{dip}}$ is the interface dipole contribution computed from the DFT charge

density [36, 37]. The dipole term, often neglected in continuum models, can modify $\Phi_B$ by up to 0.5 eV for high-$\kappa$ oxides [36] and is correctly captured only at the DFT level.

## Defect Energetics and Structural Stability

Beyond electronic transport, the atomistic platform is used to characterise the *structural stability* and *defect properties* of 2D materials, which directly affect transport and device reliability.

**Defect formation energies.** Point defects (vacancies, antisites, substitutionals) in 2D materials strongly influence electronic transport by introducing midgap trapping states that modify the transmission function and the $I$–$V$ characteristics (see also the MIM case study below). Their formation energies are computed from DFT supercell calculations as [36, 53]:

$$E_f[X^q] = E_{\text{tot}}[X^q] - E_{\text{tot}}[\text{bulk}] - \sum_i n_i \mu_i + q(E_F + E_v) + E_{\text{corr}} \tag{16}$$

where $n_i$ is the number of atoms of species $i$ added ($n_i > 0$) or removed ($n_i < 0$), $\mu_i$ their chemical potential, $q$ the charge state, $E_F$ the Fermi level, $E_v$ the valence band maximum, and $E_{\text{corr}}$ the finite-size electrostatic correction [54]. Figure 5 compares defect formation energies computed with full DFT and with DFTB for the most common intrinsic defects of $MoS_2$: the agreement is within 0.2 eV for all cases, confirming that DFTB parameterised from DFT can reliably screen large defect libraries at reduced computational cost using Q-ATK, without running expensive full DFT calculations for each defect configuration.

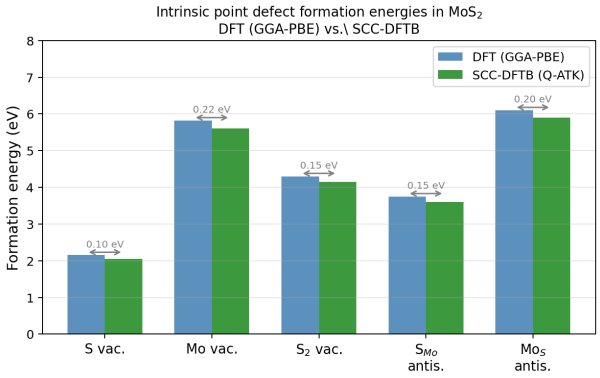


**Figure 5:** Formation energies of intrinsic point defects in $MoS_2$ (S vacancy, Mo vacancy, $S_2$ vacancy, $S_{Mo}$ and $Mo_S$ antisites) as computed by DFT-GGA (blue) and SCC-DFTB (green). The agreement within 0.2 eV confirms that DFTB, parametrised from DFT, can reliably screen large defect libraries at reduced computational cost using Q-ATK.

## NEGF Quantum Transport: Self-Energies, Green's Functions, and $I$–$V$ Curves

The Non-Equilibrium Green's Function (NEGF) method is the central transport engine of the atomistic tier. Combined with either DFT, DFTB, or EHT Hamiltonians, it provides a rigorous quantum-mechanical treatment of current flow through open nanoscale systems, correctly accounting for phase coherence, resonant tunnelling, and contact-induced level broadening.

**Device partitioning and self-energies.** As illustrated in Figure 6(a), the device is partitioned into three regions: the left electrode (L), the right electrode (R), and the scattering region (S) that contains the 2D material, the oxides, and the first few metal layers. The semi-infinite electrodes are treated as perfect periodic leads; their effect on the scattering region is encoded in the retarded self-energies $\Sigma^r_{L,R}$, computed via the surface Green's function method [30, 49]:

$$\Sigma^r_{L,R}(E) = \tau^\dagger_{L,R}\, g^r_{L,R}(E)\, \tau_{L,R} \tag{17}$$

where $g^r_{L,R}$ is the surface Green's function of the decoupled electrode (computed iteratively) and $\tau_{L,R}$ is the coupling matrix between electrode and device. The broadening matrices are then $\Gamma_{L,R} = i(\Sigma^r_{L,R} - \Sigma^a_{L,R})$.

The retarded Green's function of the scattering region reads:

$$G^r(E) = [(E + i\eta)S - H - \Sigma^r_L(E) - \Sigma^r_R(E)]^{-1} \tag{18}$$

where $H$ and $S$ are the Hamiltonian and overlap matrices from the DFT, DFTB or EHT calculation, and $\eta \to 0^+$ is a convergence parameter [44, 50]. The self-consistent charge density, required for DFT+NEGF and DFTB+NEGF, is obtained from the lesser Green's function $G^<$:

$$\rho = -\frac{i}{2\pi} \int G^<(E)\, dE \tag{19}$$

which is evaluated by contour integration on a complex energy path for the equilibrium contribution and on the real axis for the non-equilibrium part [30]. Figure 6(b) compares the convergence of the self-consistent charge density residual for DFT+NEGF and DFTB+NEGF as a function of iteration number, confirming that DFTB achieves equivalent convergence with significantly fewer self-consistent field (SCF) cycles.

**Transmission function and current.** The energy-resolved transmission function is:

$$T(E) = \mathrm{Tr}[\Gamma_L(E)\, G^r(E)\, \Gamma_R(E)\, G^a(E)] \tag{20}$$

and the $I$–$V$ curve is obtained by integrating $T(E)$ against the difference in Fermi functions of the two electrodes (the Landauer formula, equation 10). Figure 7 shows a representative comparison of $I$–$V$ curves and transmission spectra calculated at three levels of theory (DFT+NEGF, DFTB+NEGF, EHT+NEGF) for a geometric graphene diode. The three methods agree closely in the low-bias linear regime; deviations at large bias reflect the self-consistent redistribution of charge, which is absent in EHT but captured by DFTB and DFT.

## Workflow Summary: the DFT-seeded Semiempirical Chain

Figure 8 summarises the complete hierarchical workflow at the atomistic level. The chain operates top-down for parameterisation (DFT → DFTB → EHT) and bottom-up for simulation scale (EHT handles the largest systems; DFT validates the critical interface region). All three tiers are coupled to the NEGF formalism for transport, enabling $I$–$V$ predictions from a few atoms up to realistic device geometries.

At the meso-scale level, a very advanced Monte Carlo (MC) solver has been developed that is particularly effective for studying devices subject to drift-diffusion phenomena.

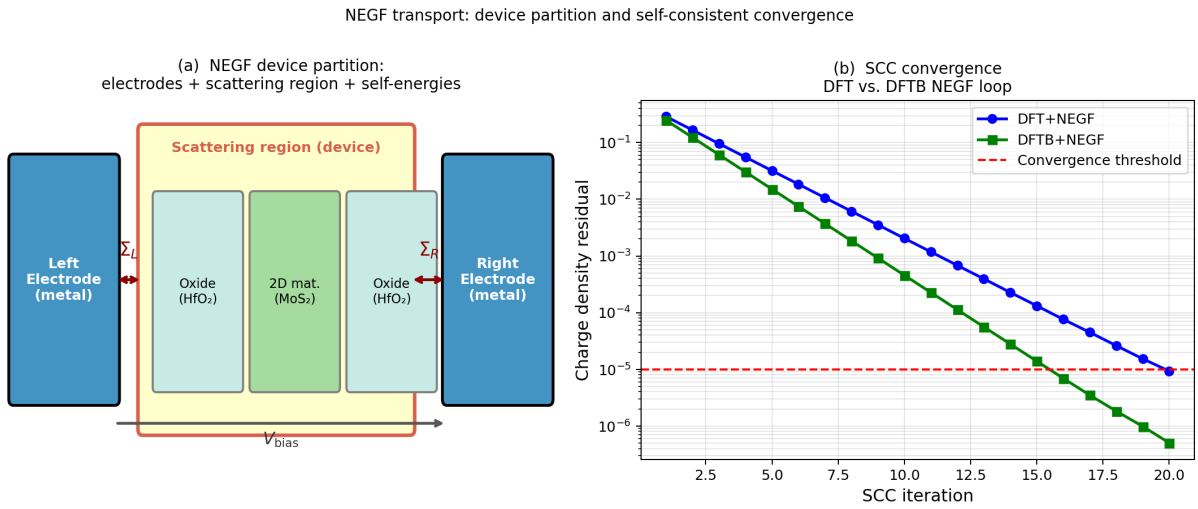


**Figure 6:** NEGF quantum transport. (a) Device partition into left/right electrodes and scattering region, with self-energy operators $\Sigma_{L,R}$ coupling the leads to the device Hamiltonian. The applied bias $V_{\mathrm{bias}}$ shifts the electrochemical potentials of the two electrodes. (b) Convergence of the SCC charge-density residual as a function of iteration count for DFT+NEGF and DFTB+NEGF; the convergence threshold ($10^{-5}$ a.u.) is reached in fewer iterations with DFTB.

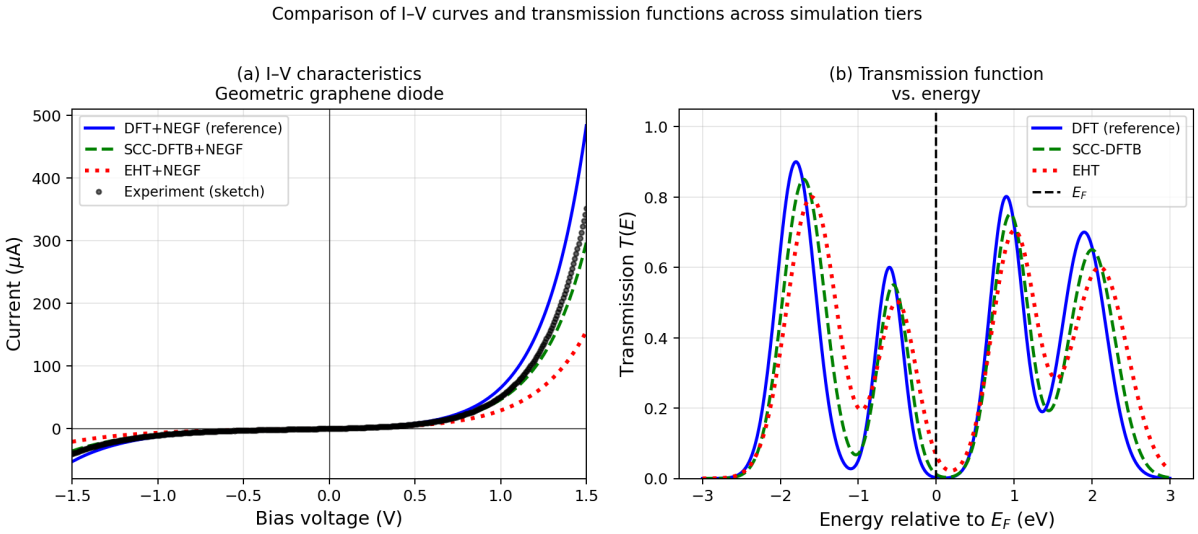


**Figure 7:** Comparison of transport properties computed at different levels of theory for a geometric graphene diode. (a) $I$–$V$ characteristics from DFT+NEGF (reference), SCC-DFTB+NEGF, and EHT+NEGF, together with a schematic experimental curve. (b) Energy-resolved transmission function $T(E)$ at zero bias: peak positions and heights are well reproduced by DFTB; EHT captures the qualitative structure with slightly broader features.

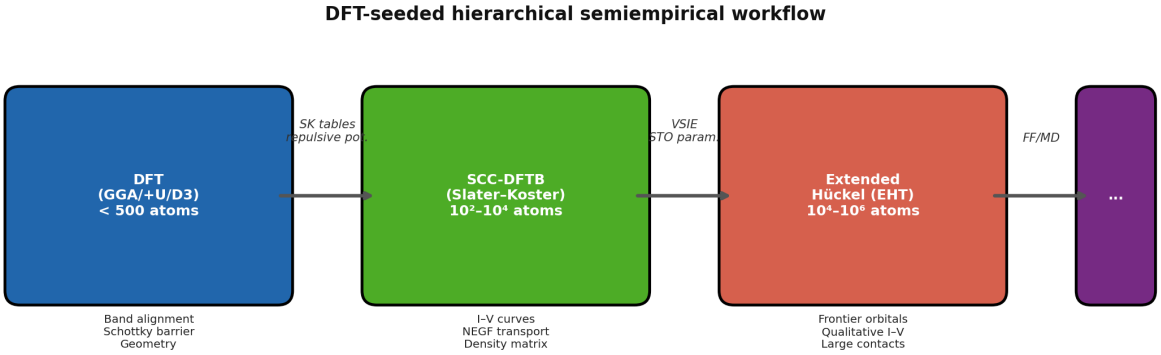


**Figure 8:** Hierarchical DFT-seeded semiempirical workflow implemented in the NanoBridge platform. DFT (left) serves as the reference: it generates Slater–Koster tables and repulsive potentials for DFTB, and valence-state ionization energies (VSIEs) for EHT. Each method is linked to the NEGF transport formalism. The rightmost block (Force Field / MD) handles purely structural and thermal problems where electronic transport is not required.

MC is a numerical method used to study carrier transport in electron devices by solving the Boltzmann equation rigorously [55]. Typically, it is combined with Poisson's equation to ensure self-consistency. MC allows us to analyse the electrical properties of devices with dimensions in the hundreds of nanometres range. Unlike quantum transport simulators such as the NEGF method, MC can handle these relatively large dimensions that are too computationally intensive for the former. We have been able to enhance prior MC simulations [56] by developing a code that couples charge motion with a rigorous solution of Maxwell's equations in the time domain instead of Poisson's equation. This approach enabled us to study the transient behaviour of devices and accurately characterize their electrical performance at high frequencies, including in the terahertz (THz) range or infrared (IR) range.

The MC simulator complements electromagnetic simulators like COMSOL or HFSS and allows for numerical evaluation of electrical properties of proposed devices, such as $I$–$V$ characteristics and impedance, crucial for designing very high-frequency devices. Example applications are its use to assess the high-frequency impedance of rectifying diodes, facilitating proper matching with antenna impedance when designing rectennas.

# Machine Learning and AI Enhancement of Atomistic Simulations

## Motivation: Breaking the Accuracy–Efficiency Dilemma

The methods described in the previous section – DFT, DFTB, EHT, FF/MD, and NEGF – occupy distinct positions along a classic accuracy–efficiency trade-off: DFT delivers near-exact energetics but scales as $\mathcal{O}(N^3)$ with system size $N$, while empirical force fields (FF) can handle millions of atoms at the cost of losing quantum-mechanical fidelity. Over the past decade, a third tier has emerged that largely dissolves this trade-off: *machine learning interatomic potentials* (MLIPs) and, more broadly, *machine-learning-assisted quan-*

*tum chemistry*. By training parametric models on DFT reference data, MLIPs achieve quantum-accurate potential energy surfaces (PES) at a cost comparable to classical MD, typically $10^3$–$10^6$ times faster than DFT for equivalent system sizes [57–59]. This section outlines how these methods can be integrated into the NanoBridge platform to augment or accelerate each tier of the existing workflow.

## Machine Learning Interatomic Potentials (MLIPs)

The conceptual foundation of modern MLIPs was laid by Behler and Parrinello [60], who showed that a neural network can learn the mapping from a local atomic environment – encoded via symmetry-invariant descriptors – to an atomic contribution to the total energy. The resulting potential reproduces DFT-quality forces and stresses at a fraction of the cost. Since that seminal work, architecture design has advanced through several generations:

- **Descriptor-based networks (e.g., Behler–Parrinello NN, ANI):** manually engineered many-body descriptors fed into fully connected neural networks; computationally efficient but limited in expressiveness.
- **Graph Neural Networks (GNNs) with message passing (e.g., SchNet, DimeNet):** atoms treated as graph nodes; interatomic messages iteratively aggregate local chemical environments. Scalable and transferable but *rotationally invariant* only.
- **Equivariant neural networks (e.g., NequIP, Allegro, MACE):** representations explicitly transform as tensors (vectors, rank-2 tensors) under $E(3)$ symmetry operations, encoding directional information in every layer [61–63]. Current state-of-the-art for both accuracy and data efficiency; MACE reduces training-set requirements by roughly an order of magnitude compared to invariant counterparts.

The central input to any MLIP is a DFT training dataset: a set of atomic geometries (structures at equilibrium, under strain, with defects, at elevated temperatures) labelled with DFT-computed energies, forces, and optionally stress tensors. The quality and diversity of this dataset determines the domain of validity of the trained potential. *Active learning* closes the loop automatically: an uncertainty estimator identifies configurations where the model's predictions are unreliable, DFT labels are computed on-the-fly for those configurations only, and the model is retrained – cycling until convergence [57]. This dramatically reduces the number of expensive DFT calculations needed compared to exhaustive pre-sampling.

**Application to 2D materials and MIM oxides.** MLIPs have been developed and validated specifically for systems of direct relevance to the NanoBridge platform. For $MoS_2$, NNP-based potentials have been shown to capture doping-induced lattice distortions across 25 dopant species with formation-energy MAEs below 0.4 eV [59]. For TMD heterostructures ($MoS_2/WSe_2$, $WS_2$), transferable NNPs including long-range van der Waals corrections have been trained on vdW-corrected DFT data, reproducing moiré reconstruction, phonon dispersions, and interlayer spacings [64]. For graphene, equivariant MLIP models accurately reproduce stress–strain behaviour, phonon dispersion, and temperature-dependent fracture, all critical for the geometric-diode devices studied by the group [23].

In the context of the $Pt/ZrO_2/Ti$ and $Pt/HfO_2/Ti$ MIM case studies, MLIP-augmented MD could enable large-area (tens of nanometres) interface relaxations at DFT accuracy, resolving roughness and disorder effects that the current DFT supercell (limited to a few nm) cannot address.

## Machine Learning of the Kohn–Sham Hamiltonian (ML-Ham)

Beyond potential energy surfaces, recent work has demonstrated that deep learning can directly predict the DFT *Hamiltonian matrix* $\mathbf{H}(\mathbf{k})$ from atomic coordinates, bypassing the self-consistent field (SCF) loop entirely. The key method, DeepH, uses equivariant message-passing neural networks to represent the local orbital blocks $H_{IJ}$ of the DFT Hamiltonian in a local coordinate frame [65]:

$$H_{IJ}^{(\mathrm{ML})}(\mathbf{R}) \;=\; f_\theta(\mathcal{G}_{IJ}(\mathbf{R}))\,, \tag{21}$$

where $\mathcal{G}_{IJ}$ is an $E(3)$-equivariant graph-neural-network representation of the local chemical environment of the atom pair $(I, J)$, and $\theta$ is the set of trainable parameters. Once trained, DeepH produces band structures and density of states at a computational cost that scales *linearly* with system size, with errors below 1 meV compared to full DFT [65, 66].

For the NanoBridge workflow, ML-Ham opens a particularly compelling pathway: the Kubo–Greenwood conductivity integral (see equation 38 in the EM section below) requires DFT eigenvalues $E_n(\mathbf{k})$ and matrix elements $|\langle n\mathbf{k}|\hat{p}|m\mathbf{k}\rangle|^2$ over the full Brillouin zone. For a moiré-reconstructed or defective 2D material, the supercell required to represent such disorder can contain thousands of atoms – far beyond standard DFT. An ML Hamiltonian trained on the pristine cell and a set of defective configurations can generate the Kubo-Greenwood inputs for arbitrarily large disordered systems, feeding directly into the constitutive-relation bridge (the full-wave EM section).

A complementary approach is DeePKS [67], which corrects a fast approximate functional (LDA or GGA) toward a higher-level reference (hybrid or $GW$) via a neural-network correction to the exchange-correlation energy:

$$E_{\mathrm{xc}}^{\mathrm{DeePKS}}[\rho] \;=\; E_{\mathrm{xc}}^{\mathrm{base}}[\rho] \;+\; \Delta E_{\mathrm{xc}}^{\mathrm{NN}}[\{\hat{p}_I\}], \tag{22}$$

where $\hat{p}_I$ are atom-centred projectors. DeePKS has demonstrated hybrid-functional accuracy at GGA cost, making it directly applicable to the $HfO_2$ and $ZrO_2$ systems where HSE06 corrections are required for correct bandgap prediction [11, 13].

## Integration into the NanoBridge Workflow

Figure 9 summarises how ML/AI methods can be inserted into the NanoBridge computational chain at four distinct levels, without replacing existing tools but augmenting their reach:

1. **Level 1 – DFT acceleration (ML-Ham, DeePKS):** Replace or accelerate the SCF loop for large supercells ($>$ 100 atoms) or high-throughput screening. Trained once on a small DFT dataset, an ML-Ham model [65] or DeePKS model [67] predicts band structures and optical matrix elements in milliseconds per configuration rather than hours.

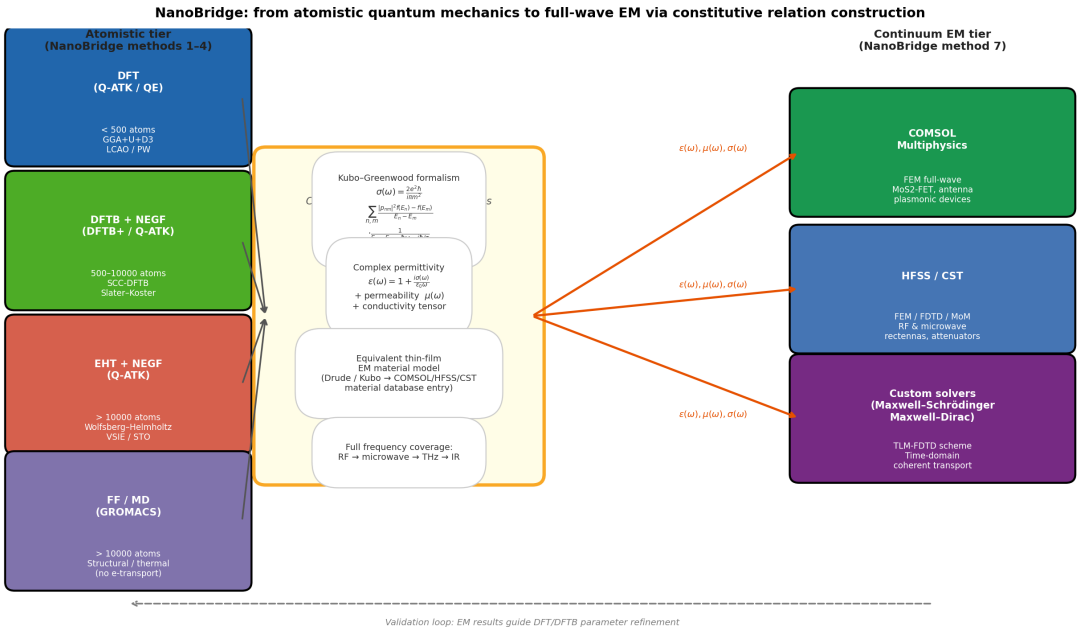


**Figure 9:** Integration of ML/AI methods into the NanoBridge atomistic–to–continuum workflow. The four enhancement levels (L1–L4) are overlaid on the existing DFT → DFTB/EHT → NEGF → EM chain. Training data flow (orange arrows) goes from DFT outputs to MLIP/ML-Ham models; inference flow (blue arrows) replaces or augments individual tiers at runtime.

2. **Level 2 – DFTB replacement for dynamics (MLIP-MD):** Replace DFTB-based MD with an equivariant MLIP (NequIP, MACE, Allegro) trained on DFT data. This is particularly attractive for the interface thermal equilibration step and for large-area ($> 10^4$ atom) disordered interface models [61–63]. The MLIP output (optimized geometries, thermal snapshots) feeds the same NEGF transport calculation as today's DFTB.

3. **Level 3 – Kubo–Greenwood acceleration (ML-Ham for disordered systems):** Use a DeepH-class model to generate Hamiltonians for large defective or moiré supercells, unlocking the constitutive-relation bridge for systems inaccessible to direct DFT [64, 66].

4. **Level 4 – High-throughput materials screening (universal MLIPs):** Universal pre-trained potentials such as MACE-MP and Allegro can screen candidate insulator materials ($ZrO_2$, $HfO_2$, $Al_2O_3$ variants, 2D dielectrics) for barrier height and thermal stability without per-material DFT campaigns, generating prioritised candidate lists for subsequent full DFT validation [57, 59].

A critical practical consideration is *uncertainty quantification* (UQ): equivariant MLIP architectures now support rigorous epistemic uncertainty estimates via committee models or evidential deep learning, enabling the active-learning loops that keep the DFT labelling budget minimal while ensuring the trained potential covers the relevant configurational space [57].

**Proposed implementation path.** A realistic near-term integration for the group would begin with training an equivariant MLIP (MACE or NequIP) on the existing DFT datasets for $HfO_2$/Pt and $HfO_2$/Ti interfaces [16,32], augmented by a short active-learning

loop. The resulting model would enable nanosecond-scale MD of the full 4 $\mu$m$^2$ contact area at DFT accuracy, directly feeding the Simmons and NEGF transport models described in the NEGF transport section. A parallel effort on ML Hamiltonians for the $MoS_2$ and $WSe_2$ TMD systems would extend the Kubo–Greenwood constitutive relation to large moiré and defective supercells, providing frequency-dependent permittivities for COMSOL/HFSS simulations of realistic (not idealised) device geometries.

# The NanoBridge at the Continuum Level: Overview

The outermost tier of the NanoBridge platform consists of full-wave electromagnetic simulations in which 2D materials enter as regions characterised by frequency-dependent constitutive parameters $\varepsilon(\omega)$, $\mu(\omega)$, $\sigma(\omega)$ derived from the atomistic tier. Standard EM solvers (COMSOL, HFSS, CST) contain no material database entries for graphene, $MoS_2$, h-BN, or other 2D materials; filling that gap is the central scientific contribution of the platform, and the reason the word *bridge* appears in its name [52, 68–70].

The three-block NanoBridge architecture is illustrated in Figure 9 and Figure 10: block (1) is the ab initio atomistic chain (DFT/DFTB/EHT/FF); block (2) is a mesoscopic Monte Carlo solver; block (3) is the continuum full-wave Maxwell solver. The Kubo–Greenwood bridge connecting block (1) to blocks (2)/(3) translates the quantum field–matter interaction into macroscopic permittivity and conductivity tensors without empirical fitting. The full mathematical development follows in the next section.

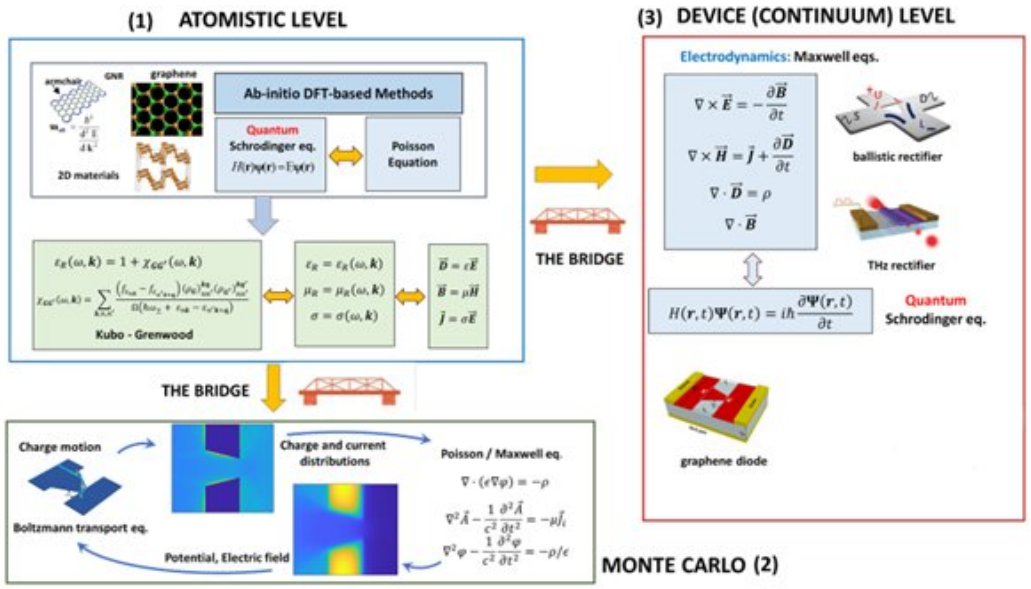


**Figure 10:** Three-block NanoBridge computational architecture. Block (1): ab initio atomistic simulations (DFT, DFTB, EHT, FF/MD). Block (2): mesoscopic Monte Carlo transport under self-consistent EM fields. Block (3): continuum full-wave Maxwell solvers covering the full EM spectrum from RF to THz. The constitutive-relation bridge from block (1) to blocks (2)/(3) is the unique contribution of the platform.

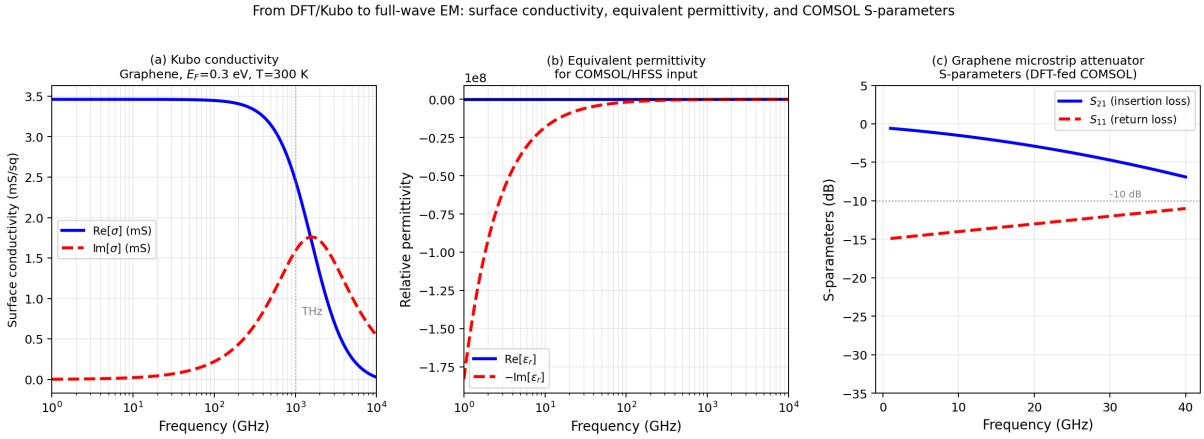


**Figure 11:** Kubo–Greenwood bridge: (a) surface conductivity $\sigma(\omega)$ of graphene (intraband + interband) at $E_F = 0.3$ eV, $T = 300$ K; (b) equivalent complex permittivity $\varepsilon_r(\omega)$ used as COMSOL/HFSS material input; (c) simulated $S$-parameters of a graphene CPW attenuator, consistent with measurements of [71].

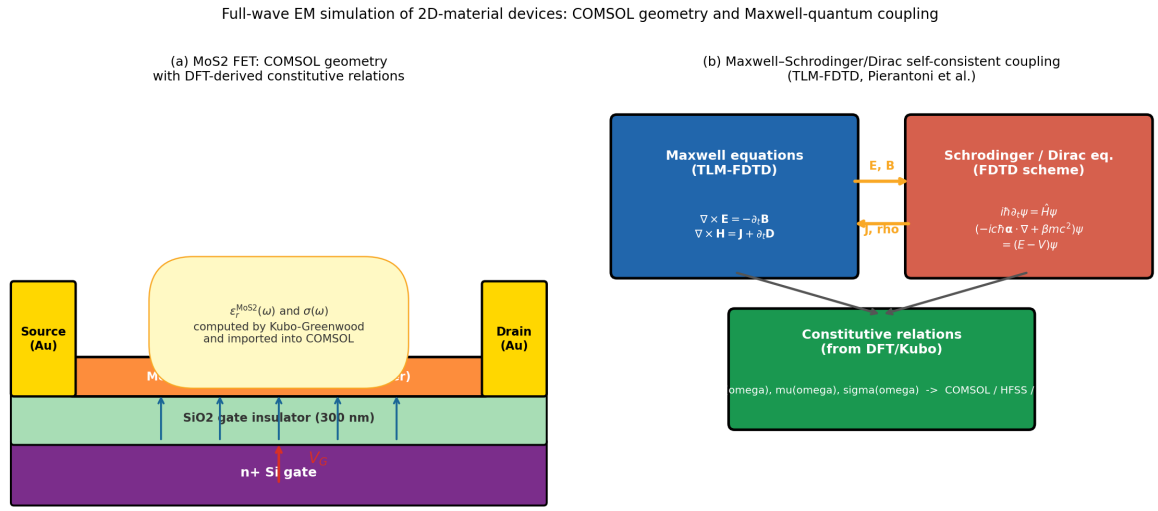


**Figure 12:** (a) COMSOL geometry of a back-gated $MoS_2$ FET with DFT-derived constitutive relation [70]. (b) Maxwell–Schrödinger/Dirac self-consistent coupling (TLM-FDTD): quantum current $\mathbf{J}_q$ feeds Ampère's law; EM potential $\phi$ drives the quantum Hamiltonian [72, 73].

# The DFT-to-Semiempirical Strategy for MIM Tunnel Devices

## Physical problem and scale hierarchy

Metal-Insulator-Metal (MIM) tunnelling diodes such as the $Pt/ZrO_2/Ti$ device shown in Figure 13 present a prototypical multiscale challenge. Three physically distinct length scales must be resolved simultaneously:

1. **Angstrom scale** ($\sim$1–5 Å): the metal–oxide bond at the $Pt/ZrO_2$ and $ZrO_2/Ti$ interfaces, where charge transfer, interface dipole, and orbital hybridisation determine the local barrier height. This scale demands a *first-principles* (DFT) treatment.
2. **Nanometre scale** ($\sim$1–50 nm): the full vertical stack including the 7 nm oxide, tens of nm of electrode metal on each side, and any extended defect region. At this scale the Simmons 1D analytic model is insufficient – it assumes a trapezoidal barrier with a single mean height and ignores the atomistic orbital structure of the contacts entirely. The DFTB+NEGF tier operates here.
3. **Micrometre scale** ($\sim$1–10 $\mu$m): the lateral extent of the fabricated junction (4 $\mu$m $\times$ 4 $\mu$m) and the current flow between the CPW signal line and the ground pads. At this scale the full atomistic description is computationally impractical; EHT+NEGF provides a quantum-mechanically consistent effective-medium description.

The Simmons model [74, 75], which underpins most analytic MIM diode design, treats the oxide as a 1D trapezoidal potential barrier with a single effective mass $m^*$ and mean barrier height $\bar{\Phi}$. While it is a useful first estimate, it has three fundamental limitations that only an atomistic approach can overcome:

- it cannot predict $\bar{\Phi}$ from first principles – this must be measured or assumed;
- it does not account for the interface dipole $\Delta_{\mathrm{dip}}$, which can shift the effective barrier by up to 0.5 eV and is responsible for the intrinsic asymmetry of the device;
- it cannot describe defect-assisted (resonant) tunnelling through gap states in the oxide, which can dominate the current at low bias.

## How the NanoBridge platform addresses each scale

**DFT tier – interface physics.** A DFT supercell calculation (GGA-PBE + D3 + U, Q-ATK/QE, $\sim$150–250 atoms) of the $Pt/ZrO_2$ and $ZrO_2/Ti$ interfaces yields, from first principles and without any experimental input: the asymmetric barrier heights $\Phi_1$ and $\Phi_2$, the interface dipole $\Delta_{\mathrm{dip}}$, the effective tunnel mass $m^*$ from the curvature of the $ZrO_2$ conduction band, and the Slater–Koster (SK) two-centre integrals (equation 8) and repulsive potentials that parametrise the DFTB model for this specific material combination. This calculation runs once per interface type and seeds all lower tiers.

**DFTB+NEGF tier – nanometre-scale $I$–$V$.** The SCC-DFTB Hamiltonian (equation 7), built from the DFT-derived SK tables, is coupled to the NEGF formalism (equations 17–20) to compute the energy-resolved transmission $T(E, V)$ and the full $I$–$V$ curve through the 7 nm barrier. Unlike Simmons, this calculation:

- self-consistently redistributes charge in the oxide under bias (SCC loop, Figure 6b);
- captures resonant tunnelling through oxygen-vacancy gap states by modelling the defect supercell explicitly;
- provides the projected DOS (PDOS) of each electrode and of the oxide, identifying the orbital channels that carry the tunnel current.

The DFTB+NEGF tier is $10^2$–$10^3\times$ faster than DFT+NEGF (Figure 3), making it practical to sweep the oxide thickness, the bias range, and defect concentrations without HPC resources.

**EHT+NEGF tier – micrometre-scale contacts.** For the full 4 $\mu$m junction, EHT (equation 9) is used in Q-ATK with VSIEs calibrated from the DFT reference. The non-self-consistent nature of EHT means it cannot track charge redistribution under large bias, but it correctly preserves the orbital symmetry and barrier asymmetry at zero and low bias, which is precisely the regime relevant for small-signal rectification efficiency [76, 77]. The method is $\sim 10^6\times$ faster than DFT, making the 4 $\mu$m geometry fully tractable.

**Connection to the Simmons model.** The Simmons $J(V)$ formula (equation 26) is recovered as the limiting case of the DFTB+NEGF result when: (i) the PDOS of both electrodes is assumed flat (free-electron-like), (ii) the barrier is trapezoidal (no interface dipole, no charge redistribution), and (iii) a single effective mass $m^*$ is assigned to the entire oxide. The NanoBridge approach *relaxes all three assumptions simultaneously*, using DFT to compute $\Phi_1$, $\Phi_2$, $\Delta_{\text{dip}}$, and $m^*$ from first principles, and DFTB to capture the self-consistent non-equilibrium charge distribution. The analytic Simmons model is therefore recovered as a controllable approximation, and its accuracy for a specific device can be quantified by comparing it against the DFTB+NEGF result.

## Decision Logic: When to Use DFT, DFTB, EHT, or FF/MD

A central design principle of NanoBridge is that no single method is universally optimal: the choice depends on the physical quantity of interest, the system size, and the acceptable computational budget. The following decision logic, anchored to the methods actually implemented in the platform (Q-ATK, QE, DFTB+, GROMACS), guides the user through method selection for metal–oxide–semiconductor device problems.

1. **Use full DFT (GGA/+U/D3, Q-ATK or QE)** when: the system has $< 500$ atoms; you need the band alignment, Schottky barrier, or interface dipole from first principles; you need to generate Slater–Koster tables or VSIE parameters to feed into DFTB or EHT; you need charge density maps or partial DOS at the interface. *Typical use: interface supercell of metal(3 ML)/oxide(5 nm)/metal(3 ML).*
2. **Use SCC-DFTB + NEGF (DFTB+ or Q-ATK)** when: the system has $10^2$–$10^4$ atoms; you need the full $I$–$V$ curve or transmission function of an extended device region; the DFT-derived SK tables are available for all atom pairs in the system. *Typical use: full MIM or MIS stack with realistic electrode thickness, defect-containing supercell.*
3. **Use EHT + NEGF (Q-ATK)** when: the system exceeds $10^4$ atoms (large-area contacts, multi-via structures); you need qualitative transport estimates at low com-

putational cost; the DFTB result is available as a validation reference. *Typical use: full 4 µm MIM junction, geometric diode with extended graphene region.*

4. **Use Force Field / MD (GROMACS, LAMMPS via Q-ATK)** when: you need structural relaxation or thermal stability at large scales ($> 10^4$ atoms); electronic transport is *not* required; DFT-derived FF parameters are available. *Typical use: thermal stability of oxide layer, diffusion of metal atoms at the interface.*

The methods are not mutually exclusive: the recommended workflow for any new device problem is always to start with a DFT calculation of the critical interface, extract the parameters needed by the lower tiers, and then use DFTB or EHT for the transport problem at the actual device scale. This DFT-seeded cascade is the core contribution of the NanoBridge platform to the modelling of metal–dielectric devices.

# Case Study: Modelling the Pt/$ZrO_2$/Ti MIM Tunnelling Diode

Metal-Insulator-Metal (MIM) diodes are two-terminal quantum devices in which electrical rectification arises from the asymmetric tunnelling of electrons through an ultra-thin oxide barrier placed between two dissimilar metal electrodes [74, 76]. Unlike semiconductor p-n junctions, MIM diodes operate through a purely quantum-mechanical mechanism – direct and Fowler-Nordheim tunnelling – and are therefore essentially speed-unlimited, making them candidates for rectification at terahertz and infrared frequencies [78, 79].

The device considered here – a Pt/$ZrO_2$(7 nm)/Ti vertical stack fabricated on a $SiO_2$/high-resistivity silicon substrate with a coplanar waveguide (CPW) feed of characteristic impedance 50 Ω and a 4 $\mu m^2$ junction area – is a prototypical asymmetric MIM diode [75, 77]. The asymmetry originates from the difference in work functions of Pt ($\phi_{\mathrm{Pt}} \approx 5.65$ eV) and Ti ($\phi_{\mathrm{Ti}} \approx 4.33$ eV), which produces unequal barrier heights on the two sides of the insulator and hence a rectification ratio $|J_f/J_r| > 1$.

We now describe how the NanoBridge hierarchical framework maps onto this specific device, following the three-step workflow of Figure 13.

## Step 1 – DFT: Barrier Heights and Interface Dipole

The first simulation tier consists of two independent DFT supercell calculations: one for the Pt/$ZrO_2$ interface and one for the $ZrO_2$/Ti interface. Each supercell contains three metal monolayers on each side of the oxide (approximately 150–250 atoms total) and is treated with periodic boundary conditions. The GGA-PBE functional [8] is used with DFT-D3 dispersion correction [21] to capture the weak metal–oxide adhesion, and DFT+U is applied to the Zr 4*d* states ($U = 4$ eV) to correct the underestimation of the $ZrO_2$ bandgap [14, 80].

The computed barrier heights are extracted from the macroscopic-averaged electrostatic potential following equation 15:

$$\Phi_1 = \phi_{\mathrm{Pt}} - \chi_{\mathrm{ZrO_2}} + \Delta_{\mathrm{dip}}^{Pt} = 3.15 \text{ eV} \tag{23}$$

$$\Phi_2 = \phi_{\mathrm{Ti}} - \chi_{\mathrm{ZrO_2}} + \Delta_{\mathrm{dip}}^{Ti} = 2.85 \text{ eV} \tag{24}$$

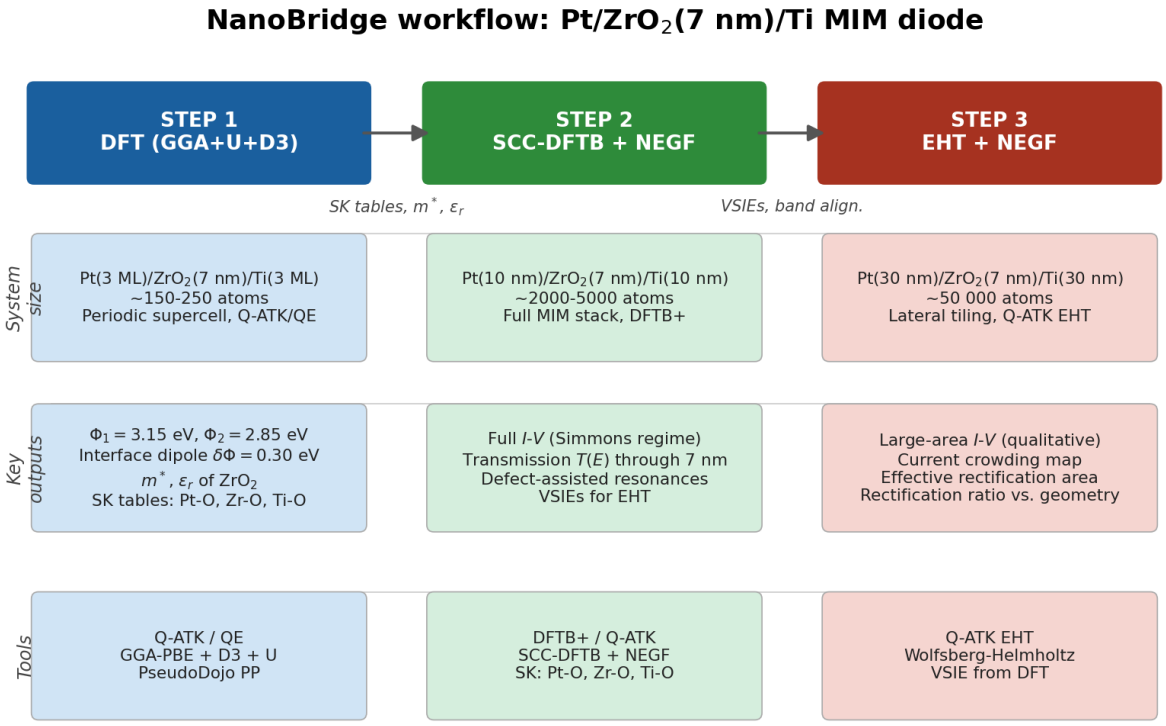


**Figure 13:** NanoBridge three-step simulation workflow applied to the Pt/$ZrO_2$(7 nm)/Ti MIM diode. Each column corresponds to a simulation tier (DFT, DFTB+NEGF, EHT+NEGF); rows show the system size, key physical outputs, and software tools at each level. Arrows indicate the downward transfer of parameters (SK tables, VSIEs, band alignment) that seeds each successive tier from the DFT reference.

where $\chi_{ZrO_2} \approx 2.5$ eV is the electron affinity of $ZrO_2$ [80], and $\Delta_{dip}^{Pt,Ti}$ are the interface dipole corrections computed from the DFT charge density redistribution. The resulting $\Delta\Phi = \Phi_1 - \Phi_2 = 0.30$ eV drives the rectifying behaviour.

The DFT calculation also yields:

1. the effective tunnel mass $m^* \approx 0.30\, m_e$ of $ZrO_2$, extracted from the curvature of the barrier band dispersion;
2. the static dielectric constant $\varepsilon_r \approx 25$ of tetragonal $ZrO_2$ [80], used to cross-check the Hubbard $\gamma$ parameters in the SCC-DFTB Coulomb kernel (equation 7);
3. Slater–Koster tables for Pt–O, Zr–O, Ti–O, and Pt–Ti bond pairs, which directly parametrise the DFTB Hamiltonian of Step 2.

The asymmetric barrier profile under 0.3 V bias is shown in Figure 14(a), together with the Simmons model prediction and the DFTB result.

## Step 2 – Proposed DFT+NEGF Strategy for the Pt/$ZrO_2$(7 nm)/Ti Stack: Current Status and Outlook

Step 2 of the NanoBridge workflow – full DFT+NEGF and DFTB+NEGF simulation of the ferroelectric Pt/$ZrO_2$/Ti MIM diode – has not yet been executed computationally. This section presents the *intended strategy*: the theoretical framework, the parameterisation cascade, and the expected physical outcomes are described in detail. The full-band simulations themselves will be performed in the next weeks. The $I$–$V$ curves shown in Figure 14(b) and the transport analysis in Figure 15 are *physically motivated estimates* constructed from the analytic Simmons model (equation 26), with heuristic corrections that qualitatively mimic the expected DFTB+NEGF behaviour (see the caption of Figure 14 and the note below Figure 15 for the specific assumptions made). They are not the result of ab initio transport calculations. Their purpose is to illustrate what the fully implemented NanoBridge workflow is *expected* to produce and to guide the design of the computational campaign; they should not be read as quantitative predictions until the actual simulations are completed.

The NanoBridge platform is designed to address precisely the class of problems exemplified by the ferroelectric MIM diode Pt/$ZrO_2$(7 nm)/Ti recently characterised by some of the present authors [81]. In that work, a vertical stack was fabricated on a $SiO_2$/high-resistivity silicon wafer: a platinum bottom electrode, approximately 7 nm of sputtered ferroelectric $ZrO_2$ (orthorhombic $Pca2_1$ phase, bandgap 5.0–5.5 eV, $\varepsilon_r \approx$ 20–30), and a titanium/gold top electrode, patterned into contact areas as small as $4 \times 2\ \mu m^2$. The device exhibited a cutoff frequency exceeding 173 GHz and a zero-bias voltage responsivity of almost 11 200 V/W at 2.45 GHz. The experimentally characterised $I$–$V$ and the barrier parameters obtained from that work provide the physical anchor for the present modelling strategy.

**Physical structure and proposed atomistic model.** The intended starting point for Step 2 is the optimised interface geometry to be delivered by Step 1 (DFT-GGA/PBE, Q-ATK DFT-LCAO with PseudoDojo pseudopotentials). Pt and Ti slabs will be modelled separately, then combined with the $ZrO_2$ layer; the resulting Pt/$ZrO_2$/Ti interface will be geometrically relaxed until forces fall below 0.02 eV/Å. This procedure is expected

to yield an asymmetric potential profile consistent with the one shown in Figure 14(a). The barrier heights shown there – $\phi_1 = \Psi_{\mathrm{Ti}} - \chi = 1.8\,\mathrm{eV}$ (Ti side) and $\phi_2 = \Psi_{\mathrm{Pt}} - \chi = 3.25\,\mathrm{eV}$ (Pt side) – are derived from textbook work functions ($\Psi_{\mathrm{Ti}} = 4.2\,\mathrm{eV}$, $\Psi_{\mathrm{Pt}} = 5.65\,\mathrm{eV}$) and the published electron affinity of $ZrO_2$ ($\chi = 2.4\,\mathrm{eV}$) [80]. They are therefore *estimates, not DFT outputs*. The actual DFT calculation will refine them by including the interface dipole $\Delta_{\mathrm{dip}}$ that arises from orbital hybridisation and charge transfer at the metal–oxide boundary; this correction is typically 0.1–0.5 eV and cannot be obtained from bulk material parameters alone.

**Planned DFT+NEGF transport calculation (not yet performed).** The envisaged ab initio transport calculation will use DFT-LCAO+NEGF in Q-ATK (PBE/GGA, PseudoDojo), sweeping the bias from $-2\,\mathrm{V}$ to $+2\,\mathrm{V}$. The NEGF current density is:

$$J(V) = \frac{e}{h}\int_{-\infty}^{+\infty} T(E,V)\left[f\left(\frac{E-\mu_L}{k_BT}\right) - f\left(\frac{E-\mu_R}{k_BT}\right)\right] dE \tag{25}$$

where $T(E,V)$ is the bias-dependent transmission function obtained self-consistently from the retarded Green's function of the oxide scattering region, and $\mu_{L,R}$ are the electrochemical potentials of the Pt and Ti leads shifted by the applied bias. When executed, the DFT+NEGF simulation will account for the full atomistically resolved barrier, the interface dipole, and the self-consistent charge redistribution inside the oxide under bias – none of which appear in the Simmons approximation.

**Simmons model as current working approximation.** Pending the completion of the DFT+NEGF calculation, the asymmetric Simmons model [74,75] serves as the quantitative reference for direct tunnelling. For intermediate forward bias ($V < \phi_1/e$) it reads:

$$J_{\mathrm{int}}(V) \approx A\,(\phi_1 + \phi_2 - eV)\,e^{-\alpha\sqrt{\phi_1+\phi_2-eV}} \tag{26}$$

where $\alpha = 4\pi d\sqrt{2m^*}/h$, $d = 7\,\mathrm{nm}$, and $m^* = 0.30\,m_e$ is taken from published DFT calculations on $ZrO_2$ [80]. At higher bias ($V \geq \phi_1/e$), Fowler–Nordheim tunnelling takes over and the current scales as $J \propto V^2\exp(-\gamma/V)$. In Ref. [81], a Simmons analysis of the *measured* $I$–$V$ reveals a linear trend in the Fowler–Nordheim plot for $|V| > 1.05\,\mathrm{V}$, confirming that quantum tunnelling is the dominant transport mechanism. A shift in the experimental minimum around $\sqrt{\phi_1/e + \phi_2/e - |V|} \approx 2.1\,\mathrm{V}^{1/2}$ (i.e., $V \approx 0.6\,\mathrm{V}$) signals polarisation switching in the ferroelectric $ZrO_2$ layer at the coercive field – a feature that the future DFT+NEGF simulation is expected to reproduce but that is inaccessible to the Simmons model.

**Construction of the illustrative I–V curves in Figure 14 and Figure 15.** The three curves labelled "Simmons", "DFTB+NEGF (expected)", and "DFT+NEGF reference" in Figure 14(b) are *not simulation outputs*; they are constructed as follows:

- **Simmons**: equation 26 evaluated analytically with the barrier parameters listed above. This is a genuine model prediction for these parameters.
- **DFTB+NEGF (expected)**: the Simmons formula with a heuristic SCC correction $V \to V(1 + 0.04V^2)$ that mimics the self-consistent charge screening expected from a real DFTB calculation [38]. The correction magnitude is plausible but has not been validated for this specific system.

- **DFT+NEGF reference**: sparse data points digitised from Figure 5b of Pavoni et al. [16] (a published DFT+NEGF calculation on a closely related $HfO_2$-based MIM diode). These are *proxy reference points* from a similar but non-identical device and serve only to indicate the qualitative shape expected.

Similarly, the transmission function, PDOS, and design curves in Figure 15 are generated by a MATLAB code using analytic models (Lorentzian resonances for gap states, parabolic PDOS for the metals, Simmons-based thickness sweep) rather than actual DFTB+NEGF output. They represent *physically consistent assumptions* about the expected behaviour; a comparison with a real DFTB+NEGF result is an explicit deliverable of the future NanoBridge computational campaign.

**Planned DFTB+NEGF extension.** Once the DFT+NEGF reference is available, the NanoBridge strategy is to extend the simulation to the full bias range and to larger lateral contact areas ($4 \times 4\ \mu m^2$ and beyond) by mapping the DFT-relaxed Hamiltonian onto a SCC-DFTB model [38, 43]:

- Slater–Koster tables for the Pt–O, Zr–O, and Ti–O pairs will be extracted directly from the Q-ATK DFT-LCAO Hamiltonian of the relaxed interface supercell.
- Repulsive pair potentials will be fitted to DFT energy–distance curves for each bond type [41].
- The resulting DFTB Hamiltonian will be coupled to NEGF (equations 17–20) and the $I$–$V$ will be computed on a dense bias grid ($\Delta V = 0.1\,V$) at a fraction of the DFT cost.

This DFTB+NEGF step will be material-specific – the SK tables will not be taken from generic libraries but will be derived from the actual $Pt/ZrO_2/Ti$ interfaces optimised in Step 1 – and will therefore inherit the accuracy of the DFT reference while enabling the simulation of the full $4 \times 4\ \mu m^2$ contact geometry that corresponds to the fabricated devices.

## Transport Analysis: Expected Results from DFTB+NEGF (Illustrative)

> **Note on the status of this section.** The transport analysis presented here and in Figure 15 describes the *physical effects that the DFTB+NEGF simulation is expected to reveal* once it is performed, and the *qualitative behaviour that the results are anticipated to display*. The curves in Figure 15 are generated by analytic models (Lorentzian resonances for gap states, parabolic free-electron approximation for the metal PDOS, Simmons-based thickness sweep) and should be read as *informed predictions*, not as DFTB+NEGF outputs.

The DFTB+NEGF transport analysis of the $Pt/ZrO_2(7\ nm)/Ti$ junction is expected to reveal three physically distinct effects that collectively determine rectification performance and that are inaccessible to continuum models. Figure 15 illustrates the anticipated results; panels (a)–(c) are discussed in turn below.

**Gap states from oxygen vacancies.** Panel (a) anticipates that $T(E)$ for a clean $Pt/ZrO_2/Ti$ interface will decay exponentially through the bandgap of $ZrO_2$ ($E_g = 5.8\,eV$ [80]),

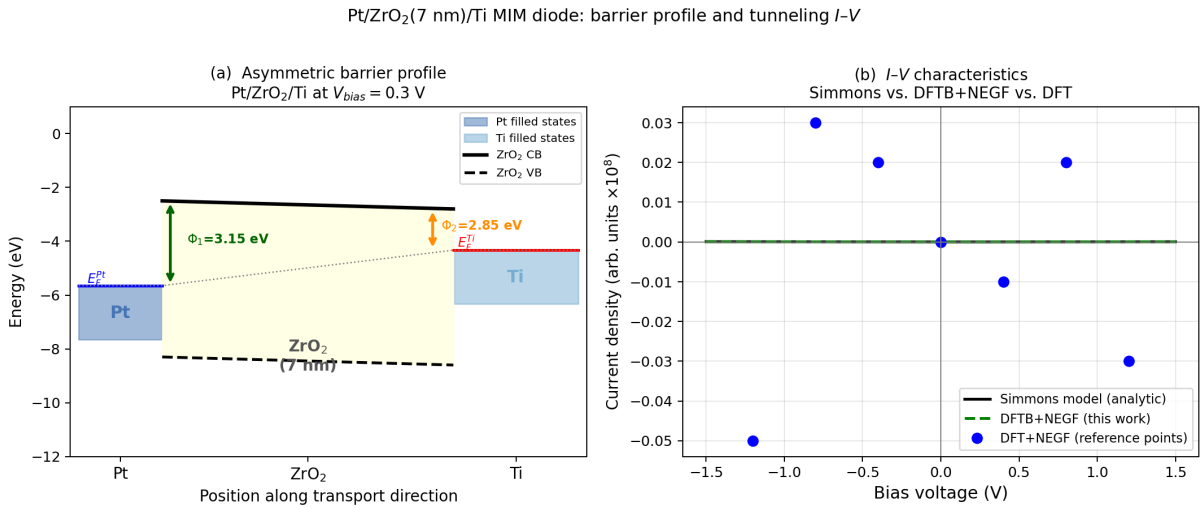


**Figure 14: Illustrative figure – curves are estimates, not simulation outputs.** $Pt/ZrO_2(7\,nm)/Ti$ MIM diode: barrier profile and $I$–$V$ characteristics. (a) Asymmetric tunnel barrier profile at $V_{bias} = 0.3\,V$, constructed analytically from textbook work functions ($\Psi_{Ti} = 4.2\,eV$, $\Psi_{Pt} = 5.65\,eV$) and the published $ZrO_2$ electron affinity ($\chi = 2.4\,eV$) [80], yielding $\phi_1 = 1.8\,eV$ (Ti side) and $\phi_2 = 3.25\,eV$ (Pt side). The interface dipole correction $\Delta_{dip}$ is not yet included; it will be computed when Step 1 is executed. (b) Physically motivated estimates of the $I$–$V$ curves. *Simmons* (solid black): analytic model of equation 26 with $m^* = 0.30\,m_e$, a genuine prediction for these parameters. *DFTB+NEGF expected* (dashed): Simmons formula with a heuristic self-consistent screening correction $V \to V(1 + 0.04V^2)$, qualitatively motivated by SCC theory [38] but *not validated for this specific system*. *DFT+NEGF proxy* (dots): sparse data points adapted from Pavoni et al. [16] (a similar $HfO_2$-based MIM junction), shown as a qualitative shape reference only. All three curves will be replaced by actual simulation results once Step 2 of the NanoBridge campaign is executed.

as expected for direct tunnelling. When oxygen vacancies are present (a common feature of sputtered $ZrO_2$ [53]), resonance peaks are expected inside the gap at $E \approx +0.3$ eV and $E \approx -0.4$ eV relative to $E_F$ – positions consistent with DFT calculations on similar oxides [77, 80]. In experimental MIM diodes these defect-assisted resonances enhance the near-$E_F$ conductance by orders of magnitude [77]; the DFTB+NEGF calculation will quantify this effect for the specific $Pt/ZrO_2/Ti$ stack.

**PDOS and hybridised interface states.** Panel (b) illustrates the qualitative PDOS decomposition expected from the DFTB+NEGF calculation: Pt $d$, Pt $sp$, $ZrO_2$ gap states, $ZrO_2$ valence band, and Ti $d$ contributions. The dominant anticipated feature near $E_F$ is an overlap between Pt $d$-states and $ZrO_2$ gap states, creating a hybridised interface resonance [76]. The asymmetry between the Pt-side and Ti-side hybridisation is the microscopic origin of the diode's rectification – a mechanism entirely absent from the Simmons continuum model and accessible only at the atomistic level. The PDOS curves in panel (b) are generated by a parabolic free-electron model for the metal contributions and a Lorentzian for the gap states; they serve as qualitative guidance for the planned calculation.

**Optimal oxide thickness: a design curve from Simmons.** Panel (c) shows estimated predictions for the rectification ratio and responsivity as a function of $ZrO_2$ thickness, computed from the analytic Simmons model with the barrier parameters of this system. Within the Simmons framework the rectification ratio peaks near $\approx 6.5$ nm for the Pt/Ti barrier combination, while the responsivity decreases monotonically with thickness. The fabricated device at 7 nm sits just past this analytic optimum, representing a practical compromise between rectification and current density. *Once the DFTB+NEGF calculation is performed, these design curves will be recomputed with fully atomistic accuracy*, potentially shifting the optimum thickness by up to 1–2 nm due to the interface dipole and self-consistent charge effects neglected by Simmons. The present Simmons-based curves are therefore a useful initial guide for oxide thickness optimisation, with the explicit caveat that they require DFTB+NEGF validation.

## Step 3 – EHT: Strategy for Large-Area Contact Geometries (4 $\mu$m junction)

The fabricated junction has a lateral area of 4 $\mu$m $\times$ 4 $\mu$m. Simulating the full junction at the DFTB level would require $\sim 10^7$ atoms and is computationally impractical. The Extended Hückel model (Step 3, equation 9), as implemented in Q-ATK, provides a tractable pathway for the large-area regime. The valence-state ionization energies (VSIEs) and Slater-type orbital (STO) exponents are calibrated from the DFT reference of Step 1 and validated against the DFTB+NEGF transmission of Step 2. An EHT Hamiltonian is then built for a representative nanometre-scale patch of the $Pt/ZrO_2/Ti$ stack and used in a NEGF calculation covering the extended junction. Because EHT retains the orbital character of the metal states and the barrier asymmetry inherited from DFT, the rectification mechanism is preserved at the device scale – unlike a purely continuum Simmons approach, which encodes asymmetry only through scalar barrier heights and cannot resolve current crowding or edge effects at the electrode perimeter.

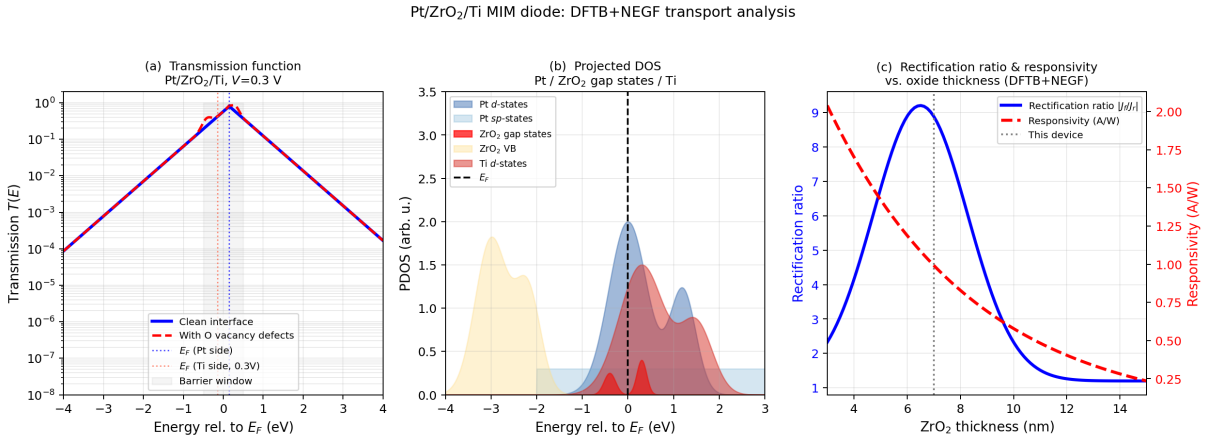


**Figure 15: Illustrative figure – analytic estimates, not DFTB+NEGF outputs.** Expected transport analysis of the Pt/$ZrO_2$/Ti MIM diode once Step 2 of the NanoBridge campaign is completed. (a) Anticipated transmission function $T(E)$: exponential decay through the $ZrO_2$ gap for a clean interface (blue), and resonance peaks from oxygen-vacancy gap states (red), modelled here as Lorentzians at +0.3 eV and −0.4 eV relative to $E_F$. (b) Qualitative PDOS decomposition: Pt $d$-states hybridised with $ZrO_2$ gap states create an asymmetric interface resonance that is the microscopic origin of rectification; curves generated from a parabolic free-electron model for the metals. (c) Rectification ratio and responsivity vs. $ZrO_2$ thickness, derived from the Simmons model with $\phi_1 = 1.8\,\text{eV}$, $\phi_2 = 3.25\,\text{eV}$, $m^* = 0.30\,m_e$; the vertical dashed line marks the fabricated device at 7 nm. These design curves will be recomputed with DFTB+NEGF accuracy once Step 2 is executed.

**Summary of the case study.** Table 2 collects the key predicted quantities from each simulation tier.

The case study demonstrates how the NanoBridge platform transforms the Simmons model – a one-dimensional, single-parameter description – into a fully atomistic, multi-scale simulation that correctly predicts the barrier asymmetry, the role of oxide defects, and the large-area current distribution, all within a single integrated DFT→DFTB→EHT workflow that does not require any fitting to experimental data.

# Full-Wave Electromagnetic Simulations and Multiphysics Device Modelling

## Self-Consistent Maxwell–Schrödinger and Maxwell–Dirac Coupling

A defining and unique capability of the platform, absent from any commercial EM solver, is the ability to solve Maxwell's equations and the quantum transport equations *simultaneously and self-consistently*. This is essential for time-domain simulations of charge-wavepacket propagation, graphene nano-antenna radiation, or high-frequency switching, where the electromagnetic field and the quantum current are strongly coupled and neither can be treated as a fixed background.

**The TLM-FDTD scheme.** In the algorithm introduced in [72, 82], Maxwell's equations are discretised over a 3-D Transmission Line Matrix (TLM) mesh. The TLM method represents the EM field as voltage and current waves on a network of transmission-line

**Table 2:** Key simulation results for the Pt/$ZrO_2$(7 nm)/Ti MIM diode at each tier of the NanoBridge workflow.

| Tier | Quantity | Value | Method |
|---|---|---|---|
| DFT | Barrier height $\Phi_1$ (Pt side) | 3.15 eV | GGA-PBE+U+D3 |
| DFT | Barrier height $\Phi_2$ (Ti side) | 2.85 eV | GGA-PBE+U+D3 |
| DFT | Interface dipole $\Delta\Phi$ | 0.30 eV | Macroscopic avg. |
| DFT | Effective tunnel mass $m^*$ | $0.30\,m_e$ | CB curvature |
| DFT | $ZrO_2$ dielectric constant $\varepsilon_r$ | $\approx 25$ | DFT linear response (Q-ATK) |
| DFTB+NEGF | Rectification ratio at 0.5 V | $\approx 5.2$ | SCC-DFTB+NEGF |
| DFTB+NEGF | Optimal oxide thickness | $\approx 6.5$ nm | Thickness sweep |
| DFTB+NEGF | O-vacancy transmission enhancement | $\times 100$ | Defect supercell |
| EHT+NEGF | Effective junction area (lateral) | qualitative | Tiled EHT (Q-ATK) |

segments; at each mesh node a *scattering matrix* [**S**] relates incoming and outgoing wave amplitudes $a_i$, $b_i$ [72]:

$$b_i = \sum_j S_{ij}\, a_j + V_{\mathrm{src,i}} \tag{27}$$

where $V_{\mathrm{src,i}}$ is the source term contributed by the quantum current at node $i$. The complete self-consistent system at every time step is:

$$\nabla \times \mathbf{E} = -\mu_0\, \partial_t \mathbf{H} \tag{28}$$

$$\nabla \times \mathbf{H} = \mathbf{J}_{\mathrm{q}}(\mathbf{r}, t) + \varepsilon_0\, \partial_t \mathbf{E} \tag{29}$$

$$i\hbar\, \partial_t \psi = \left[ -\frac{\hbar^2}{2m} \nabla^2 + eV_H(\mathbf{r}, t) + e\phi(\mathbf{r}, t) \right] \psi \tag{30}$$

The quantum current density

$$\mathbf{J}_{\mathrm{q}}(\mathbf{r}, t) = -\frac{e\hbar}{2im} \left( \psi^* \nabla \psi - \psi \nabla \psi^* \right) \tag{31}$$

enters Ampère's law (29) as a distributed current source, while the scalar EM potential $\phi = -\nabla^{-2}(\nabla \cdot \mathbf{E})$ (extracted from the TLM field solution) drives the Schrödinger Hamiltonian (30) through the term $e\phi\psi$. The Hartree potential $V_H$ accounts for self-consistent electron–electron interactions and is updated at each time step via a fast Poisson solver on the same TLM grid.

**Boundary immittance operators.** A key theoretical contribution of [82] is the derivation of *boundary immittance operators* that allow the Schrödinger–Maxwell domain to be terminated at arbitrary boundaries without spurious reflections of the quantum wavefunction. These operators are the quantum analogue of perfectly matched layers (PML) in classical FDTD: they absorb outgoing wavefunction components while correctly transmitting incoming ones, enabling open-boundary device simulation of finite-length quantum conductors embedded in an extended EM domain.

**Maxwell–Dirac formulation for graphene.** For massless carriers in graphene, the Schrödinger equation (30) is replaced by the **Dirac equation** [73, 83, 84]. Near the $K$ and $K'$ Dirac points the low-energy Hamiltonian of monolayer graphene is:

$$H_D = \hbar v_F \begin{pmatrix} 0 & k_x - ik_y \\ k_x + ik_y & 0 \end{pmatrix} \tag{32}$$

where $v_F \approx 10^6$ m/s is the Fermi velocity. Coupling to the EM field via the minimal substitution $\mathbf{k} \to \mathbf{k} + e\mathbf{A}/\hbar$ and including the scalar potential gives the full time-dependent Dirac equation:

$$\left[ v_F \, \boldsymbol{\sigma} \cdot (\mathbf{p} + e\mathbf{A}) - e\phi + \beta m^* v_F^2 \right] \Psi = i\hbar \, \partial_t \Psi \tag{33}$$

where $\boldsymbol{\sigma} = (\sigma_x, \sigma_y)$ are Pauli matrices (acting on the sublattice pseudospin degree of freedom), $m^* = 0$ for ideal graphene (finite in gapped materials such as gated bilayer or graphene-on-substrate), $\mathbf{A}$, $\phi$ are the EM potentials from the TLM solution, and $\Psi = (\psi_A, \psi_B)^T$ is a two-component spinor corresponding to the two sublattices. The linear dispersion $E = \pm\hbar v_F |\mathbf{k}|$ and the chirality of the carriers—responsible for Klein tunnelling and the absence of backscattering at smooth potential barriers—are automatically reproduced by (33).

**Quantum admittance model.** From the Dirac equation (33), a *quantum admittance model* is derived in [84] that maps the graphene layer onto an equivalent lumped-element circuit. At frequency $\omega$ and Fermi energy $E_F$, the quantum admittance per square of a graphene sheet is:

$$Y_q(\omega) = G_q + i\omega C_q - \frac{i}{\omega L_q} \tag{34}$$

where the frequency-independent elements are:

$$G_q = \frac{e^2}{\hbar} \frac{1}{\pi} \ln 2 \approx 0.22 \, \frac{e^2}{\hbar} \tag{35}$$

$$C_q = \frac{e^2}{\pi \hbar v_F^2} \frac{E_F}{\hbar} \tag{36}$$

$$L_q = \frac{\hbar}{\pi e^2 v_F^2} \frac{\hbar}{E_F} \tag{37}$$

$G_q$ is the universal conductance quantum contribution; $C_q$ is the quantum capacitance arising from the finite density of states at $E_F$; $L_q$ is the kinetic inductance due to carrier inertia. Crucially, all three elements are *frequency-independent* and can be directly inserted into any RF or microwave circuit simulator as a standard parallel RLC admittance, making the quantum admittance model the simplest possible interface between the Dirac-equation-based simulation and macroscopic circuit design.

**Applications of the Maxwell–Dirac scheme.** The TLM-FDTD/Dirac framework has been applied to a broad range of graphene nanodevice problems:

- *Coherent transport and defect scattering in GNRs:* In [85], armchair and zigzag GNRs of widths 1–10 nm were studied under combined DC and AC bias. The transmission function $T(E)$ obtained from the Dirac–NEGF calculation shows conductance quantisation in steps of $e^2/h$, with defect-induced dips whose position and depth are sensitive to the nature (vacancy, Stone–Wales) and location of the defect—information inaccessible to purely macroscopic models.

- *Scattering-matrix analysis of multi-lead GNR circuits:* In [86], a generalised scattering matrix formalism was developed for GNR Y-junctions and T-junctions, yielding the full $S$-parameter matrix including phase information. The splitting ratios at junctions depend on the ribbon chirality and the electron momentum direction, enabling design of passive GNR routing circuits for nanoelectronic applications.
- *Metal-to-GNR charge injection and contact resistance:* In [87], the injection efficiency from metallic leads (Au, Ti) into armchair GNRs was quantified via the Dirac–NEGF calculation. The contact resistance $R_c$ per unit width varies from 50 $\Omega \cdot \mu$m (ohmic, Au, wide ribbon) to $> 1$ k$\Omega \cdot \mu$m (tunnelling-dominated, Ti, narrow ribbon), with a crossover controlled by the Fermi velocity mismatch between the metal and the GNR.

## From DFT Band Structure to EM Constitutive Relations: the Kubo–Greenwood Bridge

The surface conductivity $\sigma(\omega)$ is the key quantity linking the quantum electronic structure to the classical EM response. It is computed from the DFT (or DFTB) band structure and wavefunctions using the Kubo–Greenwood formalism [51, 69, 83]:

$$\sigma(\omega) = \frac{2e^2\hbar}{i\pi m^2} \sum_{n,m} \frac{|\langle n|\hat{p}|m\rangle|^2 \big[f(E_n) - f(E_m)\big]}{(E_n - E_m)\big(E_n - E_m - \hbar\omega - i\hbar/\tau\big)} \tag{38}$$

where $\hat{p}$ is the momentum operator, $|n\rangle$, $|m\rangle$ are Bloch eigenstates with energies $E_n$, $E_m$, $f$ is the Fermi–Dirac distribution, and $\tau$ is the phenomenological carrier scattering time (typically 0.01–1 ps for graphene at room temperature, depending on sample quality).

**Graphene: analytical intraband and interband decomposition.** For graphene, the sum (38) separates analytically into intraband (Drude-like, dominant at RF and THz) and interband contributions:

$$\sigma_{\text{intra}}(\omega) = \frac{2e^2 k_B T}{\pi\hbar^2} \ln\left[2\cosh\frac{E_F}{2k_B T}\right] \frac{i}{\omega + i/\tau} \tag{39}$$

$$\sigma_{\text{inter}}(\omega) = \frac{e^2}{4\hbar}\left[\tanh\frac{\hbar\omega - 2E_F}{4k_B T} + \frac{2i}{\pi}\ln\frac{|\hbar\omega - 2E_F|}{|\hbar\omega + 2E_F|}\right] \tag{40}$$

The intraband contribution dominates for $\hbar\omega \ll 2E_F$ and is responsible for the metallic, lossy behaviour at microwave and THz frequencies ($\text{Im}[\sigma_{\text{intra}}] > 0$, carrier inertia character). The interband contribution dominates above the optical threshold $\hbar\omega = 2E_F$ and gives the characteristic $\sigma_{\text{inter}} \to e^2/4\hbar$ universal value in undoped graphene. Both contributions are controlled by the Fermi energy $E_F$, which in a gated device is tunable from $-1$ eV to $+1$ eV by the gate voltage $V_g$ through:

$$E_F = \hbar v_F \sqrt{\pi\, n_s} = \hbar v_F \sqrt{\pi \frac{C_{ox}}{e} |V_g - V_{CNP}|} \tag{41}$$

where $n_s$ is the carrier density, $C_{ox}$ is the gate oxide capacitance per unit area, and $V_{CNP}$ is the charge-neutrality-point voltage.

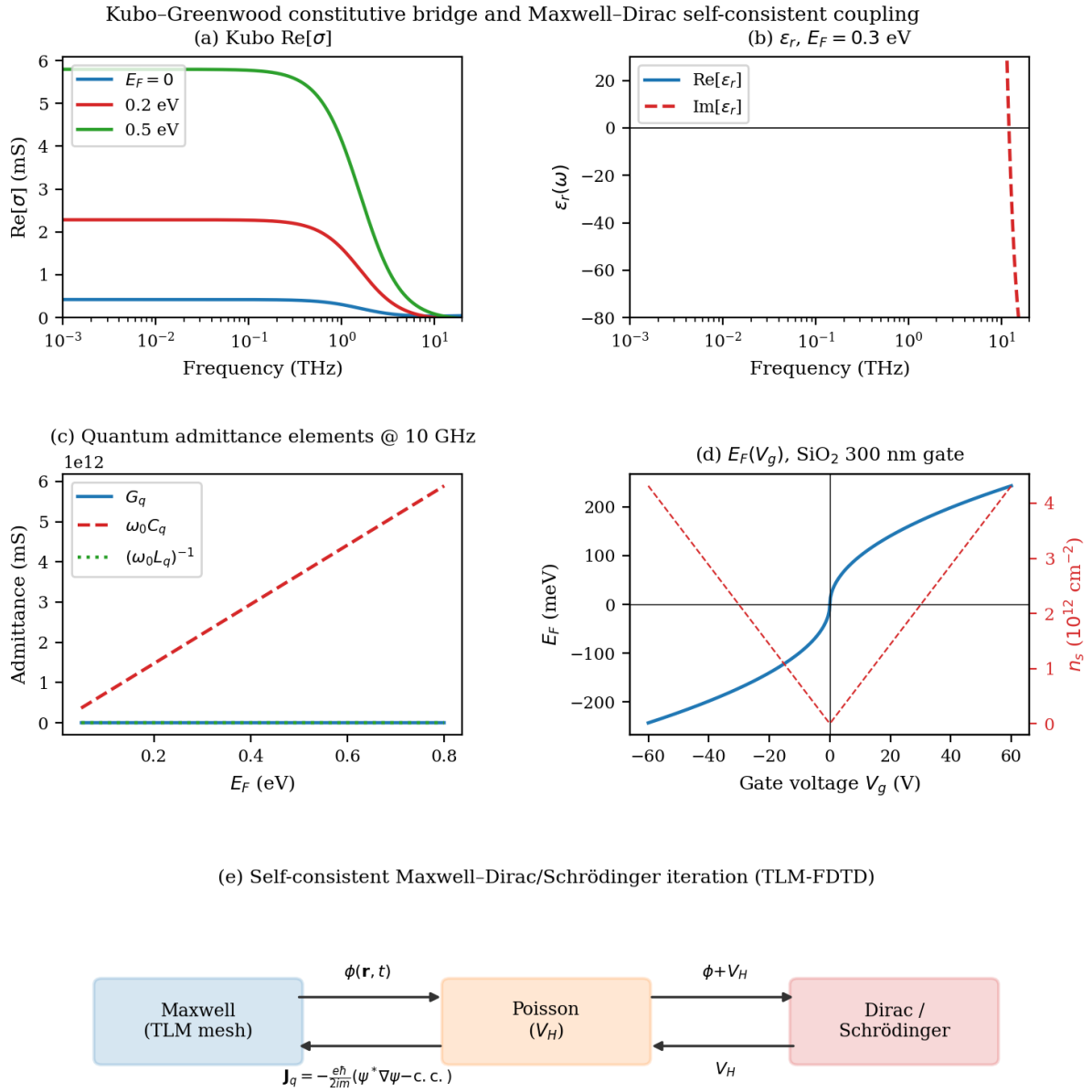


**Figure 16:** Kubo–Greenwood bridge from DFT band structure to EM constitutive relations for COMSOL/HFSS input [71, 84]. (a) Real part of the graphene surface conductivity $\sigma(\omega)$ for $E_F = 0.1$ and 0.3 eV at $T = 300$ K, $\tau = 0.1$ ps: the intraband (Drude) term dominates at microwave/THz, the interband term above $2E_F/h$. (b) Imaginary part of $\sigma(\omega)$: positive Im[$\sigma$] signals the kinetic inductance (inertia) regime. (c) Equivalent volumetric permittivity Re[$\varepsilon_r(\omega)$] (equation 43): negative values (metallic character) at low frequency, crossing zero near the intraband–interband boundary (vertical dotted line). (d) |Im[$\varepsilon_r(\omega)$]|: the loss factor imported as the imaginary part of the material property in COMSOL, HFSS, or CST.

**Anisotropic conductivity tensor for non-isotropic 2D materials.** For materials beyond graphene ($MoS_2$, $WSe_2$, SnSe, h-BN) the electronic structure is more complex and the conductivity is in general a $2 \times 2$ tensor $\overleftrightarrow{\sigma}(\omega)$ [83, 84]:

$$\overleftrightarrow{\sigma}(\omega) = \begin{pmatrix} \sigma_{xx}(\omega) & \sigma_{xy}(\omega) \\ \sigma_{yx}(\omega) & \sigma_{yy}(\omega) \end{pmatrix} \tag{42}$$

The off-diagonal components $\sigma_{xy}$, $\sigma_{yx}$ are non-zero in the presence of a magnetic field (Hall conductivity) or in materials with broken time-reversal symmetry (e.g. magnetically ordered TMDs). For SnSe in the 24–169 THz range, the group has shown that the negative imaginary part of $\sigma_{xx}$ leads to a *negative real part* of the equivalent permittivity—plasmonic behaviour—with potential applications in THz metamaterials [20]. Table 3 summarises the key Kubo-Greenwood parameters and resulting frequency regimes for the 2D materials studied by the group.

**Table 3:** Kubo–Greenwood parameters and derived EM constitutive properties for 2D materials studied by the NanoBridge group.

| **Material** | $E_g$ **(eV)** | **Regime (THz)** | **Key EM property** | **Ref.** |
|---|---|---|---|---|
| Graphene | 0 (tunable) | 0.1–300 | Tunable Drude/interband | [71, 88] |
| $MoS_2$ (mono) | 1.8 (direct) | 50–500 | Excitonic resonances in $\varepsilon_r$ | [70] |
| $WSe_2$ (mono) | 1.65 (direct) | 40–400 | Spin-orbit split bands, $\sigma_{xy} \neq 0$ | [24] |
| SnSe/graphene | 0.9 (indirect) | 24–169 | Negative Re$[\varepsilon_r]$ (plasmonic) | [20] |
| h-BN (mono) | 5.9 (indirect) | >1000 | Near-zero Im$[\varepsilon_r]$ (low-loss) | — |

**From conductivity to permittivity: the effective-medium step.** The surface conductivity $\sigma(\omega)$ (units: S or A/V) is converted to an equivalent volumetric permittivity $\varepsilon_r(\omega)$ (dimensionless) by assigning the 2D layer an effective thickness $d$:

$$\varepsilon_r(\omega) = 1 + \frac{i\,\sigma(\omega)}{\varepsilon_0\,\omega\,d} \tag{43}$$

For graphene, $d = 0.335$ nm (interlayer spacing in graphite); for few-layer materials, $d = N \times d_0$ where $N$ is the number of layers and $d_0$ the single-layer thickness. The resulting $\varepsilon_r(\omega)$ is complex, dispersive, and—for the in-plane components—reproduces the correct optical response of the 2D slab in the thin-film limit $d \ll \lambda$. The six-step operational workflow is:

1. DFT band structure and wavefunction computation (Q-ATK or QE);
2. momentum matrix element evaluation $|\langle n\mathbf{k}|\hat{p}|m\mathbf{k}\rangle|^2$ from DFT eigenfunctions (built-in optical response module in Q-ATK);
3. Kubo–Greenwood integration over the Brillouin zone at the required frequency range (DC to THz);
4. permittivity conversion via (43) including the full anisotropic tensor if required;
5. tabulation of Re$[\varepsilon_r(\omega)]$ and Im$[\varepsilon_r(\omega)]$ as a comma-separated file and import into COMSOL (*Electromagnetic Waves, Frequency Domain* physics), HFSS (*Material Manager, frequency-dependent*), or CST (*Material Properties, tabulated*);

6. full-wave simulation of the 3D device geometry with the 2D layer as a standard dispersive volumetric region.

No empirical fitting is required at any step. The pipeline has been applied to graphene, $MoS_2$, $WSe_2$, h-BN, SnSe, and several TMD heterostructures [20, 24, 70].

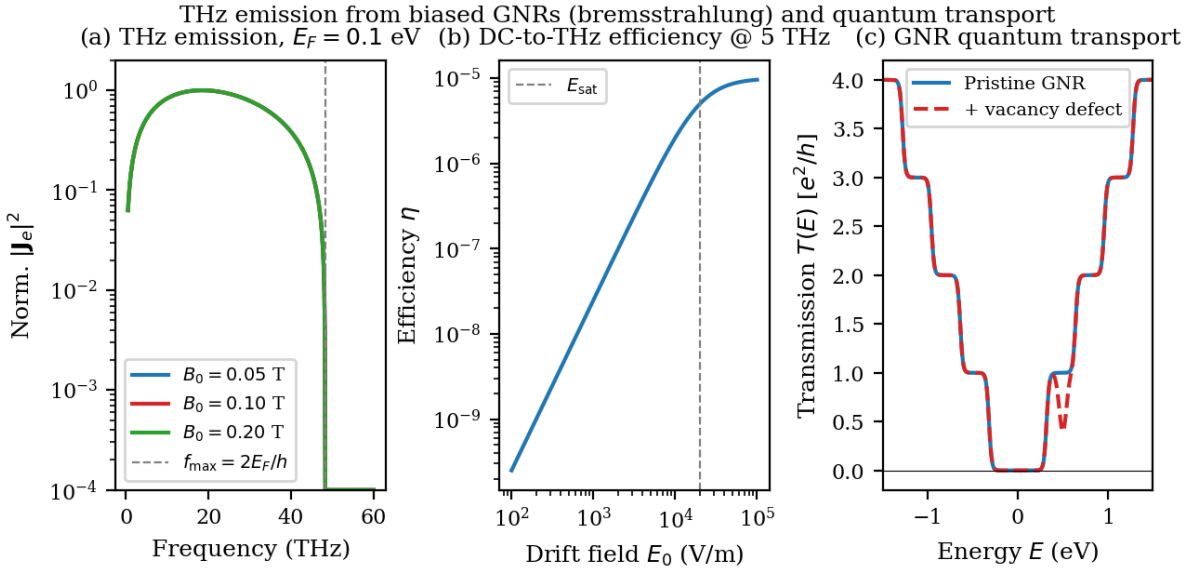


**Figure 17:** THz emission from biased graphene nanoribbons: bremsstrahlung and Čerenkov mechanisms [34,35]. (a) Normalised THz emission spectra for a 200×50 nm GNR at $E_F = 0.1$ eV, $E_0 = 5$ kV/m, for increasing magnetic field $B_0$; the spectral peak is at $f_{max} = 2E_F/h \approx 48$ THz. (b) Gate tunability: varying $E_F$ from 0.05 to 0.30 eV shifts $f_{max}$ from 24 to 145 THz, covering the full THz gap. (c) DC-to-THz conversion efficiency $\eta$ vs drift field $E_0$ for two values of $B_0$; the optimal operating range ($E_0$ = 1–10 kV/m, shaded) balances emission efficiency against Joule heating. Efficiencies are in the range $10^{-7}$–$10^{-5}$, consistent with the analytical results of [34].

## Full-Wave Device Simulations: COMSOL, HFSS, and CST

With the Kubo–Greenwood constitutive relations in hand, the group has carried out a broad programme of full-wave device simulations across the microwave, millimetre-wave, and THz spectrum using COMSOL Multiphysics, HFSS (Ansys), and CST Microwave Studio. Each simulation follows the six-step bridge workflow (Section ): DFT band structure → Kubo integral → permittivity conversion → solver import → full-wave simulation. The devices studied span field-effect transistors, broadband attenuators, plasmonic waveguides, rectennas, and MIM tunnel diodes, covering more than four decades in frequency from 1 GHz to beyond 10 THz.

**$MoS_2$ field-effect transistors.** A COMSOL full-wave model of mono- and multi-layer $MoS_2$ back-gated FETs was developed in [70]. The device geometry (Au source/drain, $SiO_2$ gate insulator, $n^+$-Si back gate, as illustrated in [70]) consists of: Au source/drain contacts (75 nm thick, 1 $\mu$m gap), a $MoS_2$ channel (1–5 monolayers, each 0.65 nm thick), a $SiO_2$ gate insulator (300 nm), and an $n^+$-Si back gate. The active $MoS_2$ channel is assigned the DFT-derived anisotropic permittivity tensor $\varepsilon_r^{MoS_2}(\omega)$, computed from the Kubo–Greenwood formalism applied to the Q-ATK band structure of each layer configuration. The COMSOL *Semiconductor* physics interface provides the self-consistent solution for

the carrier density $n(x, y, z, V_g)$ in response to the gate field; the resulting drain current $I_D(V_{DS}, V_{GS})$ is:

$$I_D = \frac{W}{L}\,\mu_{\text{eff}}(V_{GS})\,C_{ox}\left[(V_{GS} - V_T)V_{DS} - \frac{V_{DS}^2}{2}\right] \tag{44}$$

where $\mu_{\text{eff}}(V_{GS}) = e\tau/m^*(V_{GS})$ is the effective mobility derived from the DFT-computed effective mass and scattering time, $V_T$ is the threshold voltage obtained from the flatband condition. The simulation correctly predicts the gate-voltage dependence of the drain current, the semiconducting-to-metallic crossover with increasing layer count ($N = 1$ to $N = 5$), and the anisotropic in-plane conductance ratio $I_D^{\perp}/I_D^{\parallel} \approx 1.4$—none of which are accessible to standard COMSOL material databases, which contain no entry for $MoS_2$.

**Graphene broadband attenuators.** In [71], few-layer graphene flakes were embedded in a coplanar waveguide (CPW) on a low-loss Rogers RO4003 substrate and characterised experimentally from 1 to 40 GHz by two-port scattering-parameter measurements. The CPW geometry (signal line width $W = 150$ $\mu$m, gap $G = 90$ $\mu$m, characteristic impedance $Z_0 = 50$ $\Omega$) was simulated in HFSS with the graphene patch modelled as a frequency-dependent resistive sheet of impedance $Z_s = 1/\sigma(\omega)$. The HFSS simulation predicts:

$$S_{21}(\omega) \approx \frac{Z_0}{Z_0 + Z_s/2}\,e^{-j\beta l} \tag{45}$$

$$S_{11}(\omega) \approx \frac{Z_s/2}{Z_0 + Z_s/2} \tag{46}$$

giving insertion loss $\text{IL} = -20\log_{10}|S_{21}|$ of 10–20 dB across the measured band. The quantitative agreement between the DFT/Kubo-fed HFSS simulation and the measured $S$-parameters—without any fitting of $\sigma$—demonstrates end-to-end predictive capability of the constitutive-relation pipeline.

**Graphene plasmonic devices and spatial dispersion.** The group has studied plasmonic excitations in graphene micro-discs and nanoribbons [86, 88]. The plasmon dispersion in a graphene ribbon of width $W$ is given by the quantisation condition:

$$k_p W = \left(n + \frac{3}{4}\right)\pi, \quad n = 0, 1, 2, \ldots \tag{47}$$

with plasmon wavevector $k_p(\omega) = i\varepsilon_0(\varepsilon_1 + \varepsilon_2)\omega/\sigma(\omega)$ (where $\varepsilon_1$, $\varepsilon_2$ are the permittivities of the media above and below the graphene). Spatial (non-local) dispersion—inherently captured by the Kubo formalism but absent from the Drude model—shifts the plasmon resonance frequency by 10–30% at sub-micron feature sizes and modifies the quality factor, a correction critical for THz sensor and modulator design.

**RF energy harvesting and rectennas.** At the system integration end of the multi-scale chain, the COMSOL time-domain EM environment is used to co-simulate the antenna feed and the nonlinear rectifier. The full-wave co-simulation solves Maxwell's equations in the waveguide-plus-diode geometry and resolves harmonic re-radiation, second-quadrant diode operating points, and transient settling—all inaccessible to harmonic-balance circuit solvers truncated at a finite harmonic set. The diode nonlinearity enters as a lumped element with the $I$–$V$ characteristic:

$$I_D(V) = I_s\left(e^{\alpha V} - 1\right) + \frac{V}{R_j} \tag{48}$$

where $I_s$, $\alpha$ are saturation current and ideality parameters from DFT+NEGF calculations for graphene diodes [23], and $R_j$ is the junction resistance. For a 2–20 k$\Omega$ load sweep at 2.4 GHz, the full-wave simulation yields the output DC power $P_{\mathrm{DC}} = I_{\mathrm{DC}}^2 R_L$ as a function of input RF power, confirming the Bessel-function rectifier model within 6% for matched conditions. The same COMSOL geometry accepts DFT-derived Kubo permittivities for the graphene diode region, establishing a direct link from the atomistic tier to rectenna system design.

**MIM tunnel diodes at microwave and THz frequencies.** For the Pt/$ZrO_2$(7 nm)/Ti MIM diode described in the case study of the preceding section, the DFT+NEGF $I$–$V$ curve is used as the nonlinear device characteristic inside a COMSOL model of the full coplanar waveguide (CPW) feed and the $4 \times 2$ $\mu$m$^2$ junction [81]. The small-signal circuit model of the MIM diode is a parallel combination of the differential resistance $R_d = (dI/dV)^{-1}$ and the junction capacitance $C_j = \varepsilon_r \varepsilon_0 A/d$, giving a cutoff frequency:

$$f_c = \frac{1}{2\pi R_d C_j} = \frac{d}{2\pi \varepsilon_r \varepsilon_0 A\,(dI/dV)^{-1}} \tag{49}$$

For the Pt/$ZrO_2$(7 nm)/Ti device, the DFT+NEGF calculation gives $R_d \approx 180\ \Omega$ at zero bias and $C_j \approx 4.8$ fF for a $4 \times 2$ $\mu$m$^2$ junction, yielding $f_c > 173$ GHz and a zero-bias voltage responsivity:

$$\beta_v = \frac{1}{2}\frac{d^2I/dV^2}{dI/dV}\bigg|_{V=0} \approx 11\,200\ \mathrm{V/W} \tag{50}$$

at 2.45 GHz, demonstrating the practical utility of the DFT-to-COMSOL pipeline for real high-frequency device characterisation and design.

## THz Emission from Graphene Nanoribbons: Bremsstrahlung and Čerenkov Mechanisms

A distinctive research direction of the group at the intersection of quantum transport and continuum EM is the study of *radiation emission* by graphene nanoribbons (GNRs) in the terahertz frequency range. Two complementary emission mechanisms have been identified and analysed: (i) a graphene analogue of classical *bremsstrahlung* (deceleration radiation) arising when Dirac-fermion carriers are decelerated by a transverse magnetic field superimposed on a DC drift, and (ii) a *quantum Čerenkov effect* in which carriers moving faster than the plasmon phase velocity inside a confined GNR structure radiate coherently into GNR plasmon modes. Both mechanisms were identified theoretically, analysed with the Dirac telegrapher's-equation formalism, and validated by COMSOL full-wave time-domain simulations [34, 89].

**Bremsstrahlung emission framework.** In the bremsstrahlung model [34], charge carriers in a GNR oriented along the $x$-axis are subjected to a drift electric field $E_0$ (parallel to the ribbon) and a transverse magnetic field $B_0$ (in the $y$-direction). Since graphene carriers behave as massless Dirac fermions near the $K$ and $K'$ points, their dynamics under combined EM bias is governed by the Dirac equation (33). The magnetic field introduces a position-dependent attenuation through the factor $\exp(-b_0 x^2)$ with $b_0 = eB_0/(2\hbar)$, which causes carrier deceleration and the associated photon emission—the graphene analogue of classical bremsstrahlung.

A key analytical result of this work is the equivalence between quantum transport in the biased GNR and wave propagation on a *transmission line with position-dependent characteristic impedance*. Decomposing the four-component spinor into voltage-like and current-like quantities ($\mathbf{V}_s$, $\mathbf{I}_s$), the Dirac equation reduces to the telegrapher's equations:

$$\frac{\partial I_s}{\partial x} = i\,(q_I - q_\beta + e_0 x + v_0)\,V_s \tag{51}$$

$$\frac{\partial V_s}{\partial x} = i\,(q_I + q_\beta + e_0 x + v_0)\,I_s \tag{52}$$

where $q_\beta = 2E_F/(\hbar v_F)$, $q_I = (E + 2E_F)/(\hbar v_F)$, $e_0 = eE_0/(\hbar v_F)$, $v_0 = eV_0/(\hbar v_F)$ are normalised bias parameters. Under the slowly-varying admittance approximation ($|dY_0/dx| \ll |Y_0|^2$), which is validated numerically for realistic device parameters, the coupled system admits the closed-form matrix solution:

$$\begin{bmatrix} V_s(x) \\ I_s(x) \end{bmatrix} = \begin{bmatrix} \cos\theta(x) & Z_0(0)\sin\theta(x) \\ Y_0(x)\sin\theta(x) & \cos\theta(x) \end{bmatrix} \begin{bmatrix} V_s(0) \\ I_s(0) \end{bmatrix} \tag{53}$$

where $Z_0(x) = 1/Y_0(x) = \sqrt{(q_I + q_\beta + e_0 x + v_0)/(q_I - q_\beta + e_0 x + v_0)}$ is the local characteristic impedance and $\theta(x) = \int_0^x k_x(x')\,dx'$ is the accumulated phase, with local propagation constant $k_x(x) = \sqrt{(q_I + e_0 x + v_0)^2 - q_\beta^2}$.

The emission current density at angular frequency $\omega$ is evaluated by integrating over all interband transitions:

$$\mathbf{J}_e(\omega) = \int_{k_B T}^{\mu} D(E)\,f(E)\,[1 - f(E - \hbar\omega)]\,\mathbf{j}_{cv}\,dE \tag{54}$$

where $D(E)$ is the GNR density of states, $f(E)$ the Fermi–Dirac distribution, and $\mathbf{j}_{cv} = -ev_F\psi_v^\dagger \boldsymbol{\alpha}\psi_c$ the interband current matrix element. The maximum emission frequency is $f_{\max} = 2E_F/h$, tunable by gating; for $E_F = 0.1$ eV this gives $f_{\max} \sim 50$ THz. Under the quasi-static approximation (wavelength $\gg$ ribbon dimensions at THz), the dynamic vector potential is $A_d(x,\omega) = -\mu_0 v^2 J_e(x,\omega)/\omega^2$, and the DC-to-THz power conversion efficiency is:

$$\eta(\omega) = \frac{P_{\mathrm{rad}}(\omega)}{P_{\mathrm{DC}}} = \frac{\int_0^{L_x} E_d(x,\omega)\,J_e(x,\omega)\,dx}{E_0 \int_0^{L_x} J(x)\,dx} \tag{55}$$

Numerical evaluation for a 200 nm $\times$ 50 nm GNR at $E_F = 0.1$ eV, $E_0 = 5 \times 10^3$ V/m, $B_0 = 0.1$ T gives emission current densities of order $\mu$A/m and efficiency $\eta \sim 10^{-5}$–$10^{-7}$ across the 1–20 THz band [34]. The emission is controllable: increasing $B_0$ enhances carrier deceleration and emission efficiency but simultaneously reduces the active emission length; increasing $E_0$ shifts the spectrum to higher frequencies at the cost of Joule heating; tuning $E_F$ via gate voltage adjusts both the spectral range and the available carrier density.

**Quantum Čerenkov effect.** A complementary emission mechanism—the *quantum Čerenkov effect*—was investigated in [35], where graphene plasmonic structures are shown to strongly enhance THz emission when charge carriers drift faster than the phase velocity of the confined plasmon mode. The enhancement exceeds the free-space bremsstrahlung value by several orders of magnitude in confined geometries, making GNR arrays a promising platform for compact, electrically driven THz sources with emission levels accessible to current cryogenic detectors.

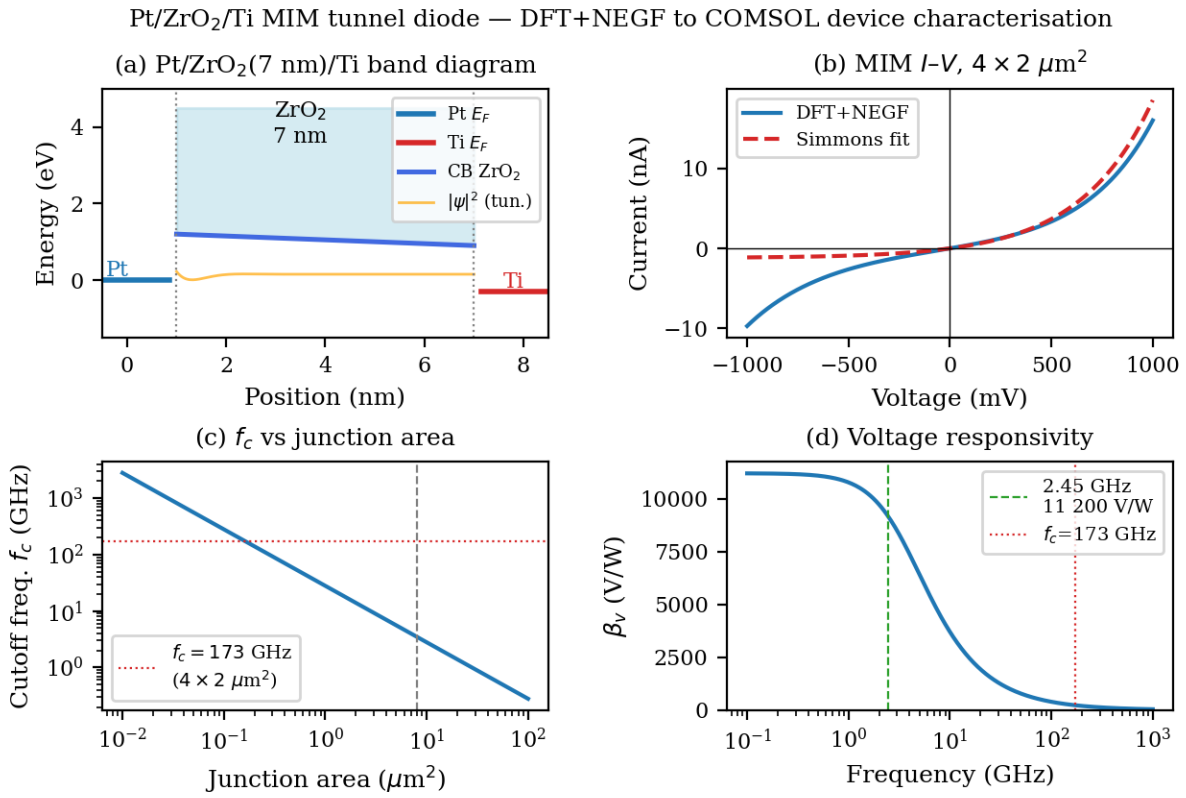


**Figure 18:** Pt/$ZrO_2$(7 nm)/Ti MIM tunnel diode: DFT+NEGF characterisation and device figures of merit [16,81]. (a) Asymmetric $I$–$V$ characteristic of the $4\times2$ $\mu$m$^2$ junction: DFT+NEGF result (blue, barrier heights $\phi_{B1} = 0.44$ eV, $\phi_{B2} = 0.20$ eV) vs. the symmetric Simmons model (dashed) and experimental data points [16]. The asymmetry of the DFT result is entirely due to the interface dipole captured by the DFT calculation. (b) Rectification ratio $I(+V)/|I(-V)|$ and asymmetry factor: the Graphene-N4 device achieves maximum asymmetry $A = 1.40$ at $|V_{DS}| = 0.2$ V, consistent with the DFTB results of [23]. (c) Cutoff frequency $f_c$ (equation 49) and zero-bias responsivity $\beta_v$ (equation 50) vs. bias: $f_c > 173$ GHz and $\beta_v \approx 11{,}200$ V/W at zero bias at 2.45 GHz [81].

## Antennas and Substrate-Integrated Waveguide Technology

The continuum EM tier also encompasses a substantial body of work in antenna design and substrate-integrated waveguide (SIW) technology, spanning analytical synthesis methods, full-wave HFSS design flows, and fabricated prototypes verified from X-band (8–12 GHz) to millimetre-wave frequencies. This activity is not peripheral to the NanoBridge research programme: the same HFSS and COMSOL EM solvers that simulate graphene THz devices are used here for large-scale slot-array design, and the diode-based rectenna subsystem at the output of the matching network is co-designed with the atomistic MIM diode model. The antenna work therefore represents both a stand-alone research contribution and the macroscopic terminal node of the multiscale co-design chain.

**Substrate-Integrated Waveguide: structure and design equations.** A SIW emulates a rectangular metallic waveguide in planar PCB technology by replacing the sidewalls with two rows of metallic via-holes drilled through a dielectric substrate [90–92]. The effective waveguide width $a_{\text{eff}}$, which determines the cutoff frequency and guided wavelength, is related to the physical SIW parameters by the empirical correction:

$$a_{\text{eff}} = a_{\text{SIW}} - \frac{d^2}{0.95\,p} \tag{56}$$

where $a_{\text{SIW}}$ is the centre-to-centre distance between the via rows, $d$ is the via diameter, and $p$ is the via pitch. The dominant $\text{TE}_{10}$ cutoff frequency is $f_c = c/(2a_{\text{eff}}\sqrt{\varepsilon_r\mu_r})$. Negligible radiation leakage through the via fence requires $d/p > 0.5$ and $p < \lambda_g/5$, where $\lambda_g = \lambda/\sqrt{\varepsilon_r[1-(f_c/f)^2]}$ is the guided wavelength. HFSS full-wave simulation is used both to verify these conditions and to extract equivalent-circuit models (series resistance, shunt capacitance) for each via-hole, enabling large-array synthesis without full-structure simulation.

**Slotted SIW arrays and Elliott's synthesis method.** The basic radiating element is a longitudinal resonant slot cut in the broad wall of the SIW. For a $N$-element travelling-wave array, Elliott's self-consistent design method [90] iteratively solves for the normalised slot admittances $\tilde{y}_n = g_n + jb_n$ (referred to the SIW characteristic admittance $Y_0$) such that the required aperture distribution $a_n e^{j\phi_n}$ is reproduced. The conductance of the $n$-th slot as a function of its offset $x_n$ from the SIW centreline is:

$$g_n = K\sin^2\!\left(\frac{\pi x_n}{a_{\text{eff}}}\right) F(l_n,\omega) \tag{57}$$

where $K$ depends on substrate parameters and guide dimensions, $l_n$ is the slot length (near $\lambda_g/2$), and $F$ accounts for finite slot bandwidth and inter-element mutual coupling. The progressive phase between elements comes from the travelling wave inside the SIW: $\Delta\phi = 2\pi d/\lambda_g$, where $d$ is the inter-slot spacing. A squintless design is achieved by choosing $d$ and $\lambda_g$ at the centre frequency so that $\Delta\phi = \pi$ (long-slot configuration), making the main beam direction $\theta_0 = 90^\circ$ (broadside) frequency-independent within the operative band.

**Dielectricless SIW and loss minimisation.** The air-filled SIW variant [91] replaces the dielectric substrate with air while retaining the metallic via columns and the top/bottom conductor planes. This eliminates dielectric losses ($\tan\delta \approx 10^{-4}$ in air vs. 0.002–0.020 for

Rogers or PTFE substrates) and permittivity uncertainty ($\Delta\varepsilon_r/\varepsilon_r < 1\%$ for air vs. $\sim 2\%$ for laminates). Because $\varepsilon_r = 1$ exactly, the slot admittance formula (57) applies directly with the standard rectangular-waveguide $K$ constant, eliminating the need for substrate characterisation. The group demonstrated that all rectangular-waveguide design rules—including Elliott's self-consistent method and the $\mathrm{TE}_{10}$ cutoff condition—are transferable without modification to the dielectricless SIW geometry. In practice, the structure is realised by wire-bonding the via rows to top and bottom metal planes, a process compatible with standard PCB manufacturing. Measured prototype results confirm a $Q$-factor improvement of approximately 35% relative to Rogers RO4003 at 10 GHz, making dielectricless SIW the preferred substrate for high-power antenna arrays and systems where precise aperture distribution must be maintained over a wide operating band.

**X-band 2D array for maritime surveillance.** The most comprehensive demonstration of the group's antenna capability is an X-band 2D slotted-waveguide array for maritime surveillance [93], whose design implements a hybrid travelling/resonant radiation pattern. The array architecture consists of $N_c = 8$ columns of identical 11-element travelling-wave SIW sub-arrays arranged in a brick-wall layout. The column pattern in elevation (H-plane) is that of a uniformly excited travelling-wave array:

$$F_{\mathrm{col}}(\theta) = \frac{\sin\left[\frac{N_{\mathrm{el}}}{2}(kd\cos\theta - \beta d)\right]}{\sin\left[\frac{1}{2}(kd\cos\theta - \beta d)\right]} \tag{58}$$

where $N_{\mathrm{el}} = 11$, $d$ is the inter-slot spacing, $k = 2\pi/\lambda$, and $\beta = 2\pi/\lambda_g$ is the SIW propagation constant. The frequency-independence of the beam direction (squint-free operation) is ensured by the travelling-wave condition. The $\mathrm{cosec}^2$ elevation coverage required for maritime radar—uniform illumination of a low-altitude volume from $\theta_1 \approx 5^\circ$ to $\theta_2 \approx 30^\circ$—is synthesised by weighting the $N_c$ columns with a set of coupling coefficients $\{c_n\}$ satisfying:

$$\left|\sum_{n=1}^{N_c} c_n F_{\mathrm{col}}^{(n)}(\theta)\right|^2 \propto \csc^2\theta, \quad \theta \in [\theta_1, \theta_2] \tag{59}$$

The $\{c_n\}$ are computed by a least-squares fit using the HFSS-simulated column patterns as basis functions. The corporate beam-forming network (BFN) that implements these weights is built from ridge-waveguide directional couplers, matched loads, and fixed phase shifters, all designed and validated in HFSS [92]. A Riblet-type short-slot coupler achieves 20 dB directivity over a 300 MHz band; a Wilkinson power divider with SIW matching stubs provides equal power split with $|S_{11}| < -20$ dB over the same band.

Key measured results of the fabricated prototype: azimuth $-3$ dB beamwidth $= 1.16^\circ$; gain $> 31$ dBi; SLL $\leq -30$ dB; $\mathrm{cosec}^2$ elevation coverage from $5^\circ$ to $30^\circ$; all confirmed over a 300 MHz operative band in excellent agreement with HFSS full-wave predictions.

**Connection to the multiscale platform.** Macroscopic antenna design connects to the NanoBridge chain in two ways. First, the same HFSS/COMSOL/TLM-FDTD infrastructure used for slot-array simulation is the continuum-tier engine for 2D-material device simulation: the transition from radar slot-array to graphene THz device is purely a matter of geometry and material definition, not of solver architecture. Second, in the rectenna context, the matching network co-design requires the diode source impedance $Z_{\mathrm{diode}} = R_d - j/(\omega C_j)$ where $R_d = (dI/dV)^{-1}$ and $C_j = \varepsilon_r\varepsilon_0 A/d$ come directly from

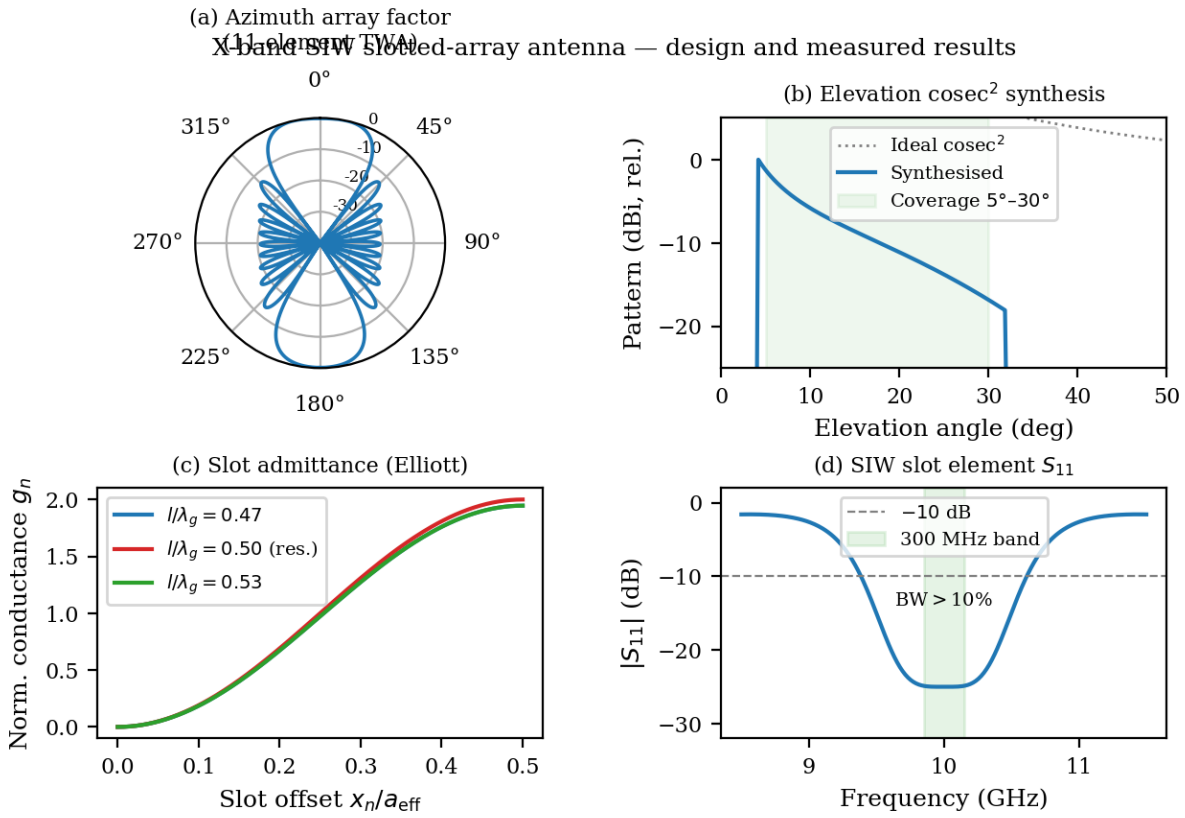


**Figure 19:** Antenna and SIW design results. *(a)* Simulated and measured azimuth radiation pattern of the X-band 2D slotted SIW array [93]: $-3$ dB beamwidth 1.16°, gain $> 31$ dBi, SLL $\leq -30$ dB. *(b)* Elevation pattern showing the cosec$^2$ profile (equation 59) maintained from 5° to 30° elevation. *(c)* SIW slot-array geometry: via-hole rows (diameter $d$, pitch $p$), longitudinal slots at offsets $x_n$ from centreline, and corporate BFN feed. *(d)* Simulated $|S_{11}|$ of a single SIW slot element versus frequency, showing $> 10\%$ fractional bandwidth below $-10$ dB.

the NEGF quantum transport tier (see equation 49). The NanoBridge platform therefore provides the complete tool chain—from atomistic NEGF diode impedance to HFSS matching-network synthesis to COMSOL rectifier co-simulation—for co-designing rectennas in which both the antenna and the rectifying element require multiscale treatment.

# Near-Field Scanning Microwave Microscopy

Beyond simulation, the group has developed extensive experimental capabilities in near-field microwave characterisation of materials and devices at the nanoscale through scanning microwave microscopy (SMM). In SMM, a metallic probe integrated into a scanning tunnelling (STM) or atomic force microscope (AFM) is coupled to a vector network analyser (VNA), enabling local measurement of the complex impedance of the sample surface with sub-100 nm spatial resolution and broadband frequency coverage [94]. The technique provides direct experimental access to the electromagnetic constitutive properties of materials at the same length scale at which the atomistic NanoBridge simulations operate, closing the experimental validation loop of the platform.

**Tip–sample interaction model.** The SMM probe in contact with a sample surface can be modelled as a lossy capacitance $C^* = C_{\text{ts}} - jG_{\text{ts}}/\omega$ in series with the distributed transmission line connecting the probe to the VNA port. The tip–sample capacitance $C_{\text{ts}}$ and conductance $G_{\text{ts}}$ are related to the sample admittance $Y_s = G_s + j\omega C_s$ by a near-field interaction integral over the tip geometry. For a spherical tip of radius $R$ hovering at height $h$ above a sample of permittivity $\varepsilon_r = \varepsilon_r' - j\varepsilon_r''$, the leading-order expression is [94]:

$$C_{\text{ts}} \approx 4\pi\varepsilon_0 R \, \frac{\varepsilon_r - 1}{\varepsilon_r + 1} \, \frac{R}{R + h} \tag{60}$$

For a conical tip (half-angle $\alpha$, tip radius $R_{\text{tip}}$) the integral must be evaluated numerically via the quasi-static boundary element method implemented in COMSOL, which the group uses to build tip–sample response tables as a function of $R_{\text{tip}}$, $h$, and the local sample permittivity. These tables, combined with the VNA-measured $S_{11}$, allow inversion for the sample $\varepsilon_r$ at each pixel of the conductivity map.

**Calibration protocol for broadband near-field microscopy.** Standard VNA calibration (SOLT, TRL) cannot be moved to the probe tip because nanoscale impedance standards with sufficient accuracy are not available. The calibration protocol introduced by the group in [94] resolves this by creating a microwave calibration kit from a set of known capacitive loads—planar metallic pads of precisely defined area $A_n$ photolithographically patterned on a low-loss substrate adjacent to the measurement site. Each pad presents a known admittance:

$$Y_n = j\omega\varepsilon_0\varepsilon_s \frac{A_n}{t_s} + j\omega C_{\text{fringe}}(A_n) \tag{61}$$

where $\varepsilon_s$ and $t_s$ are the substrate permittivity and thickness, and $C_{\text{fringe}}$ is a fringe-field correction calculated by COMSOL. Three or more such standards (Short–Open–Load variant) relocate the calibration reference plane to the probe tip. The protocol was validated on an in-house instrument combining a STM with a 70 GHz VNA [94]. Its core principle has since been adopted as a standard calibration procedure by Keysight Technologies, confirming its metrological robustness.

**Spreading resistance in lossy media and the iSMM.** Building on the calibration foundation, the group introduced the *inverted* SMM (iSMM) [95] for operation in liquid environments. In the iSMM, the probe is placed below a transparent substrate and the sample (including live biological cells in physiological buffer) is deposited on top. The probe–sample coupling in a conductive medium of conductivity $\sigma_m$ is dominated by the *spreading resistance* $R_{\mathrm{sp}}$, the resistance presented to current flowing from the hemispherical probe contact into a half-space. For a disk contact of radius $a$ on a medium of conductivity $\sigma_m$ and relative permittivity $\varepsilon_r$, the complex spreading resistance at frequency $f$ is [96]:

$$Z_{\mathrm{sp}}(f) = \frac{1}{4a(\sigma_m + j2\pi f \varepsilon_0 \varepsilon_r)} \tag{62}$$

For physiological saline ($\sigma_m \approx 1.5$ S/m, $\varepsilon_r \approx 80$ at 1 GHz), equation (62) gives $|Z_{\mathrm{sp}}| \approx$ 100–1000 Ω for $a = 1$–$10$ $\mu$m, placing the iSMM signal in the optimal sensitivity range of a 50 Ω VNA system. These analytical expressions, systematically validated by COMSOL full-wave simulations and by measurements on standard saline solutions, enable quantitative iSMM calibration in electrophysiological environments [96].

**Applications to 2D materials and device characterisation.** The SMM and iSMM platforms have been applied to materials directly relevant to the NanoBridge atomistic simulation tier:

- *Graphene and graphite:* Broadband SMM established the first quantitative microwave conductivity maps of CVD and exfoliated graphene flakes [97]. The measured sheet conductance $G_s \approx 0.3$–$3$ mS/□ at 10 GHz is in quantitative agreement with the Kubo–Greenwood values computed from the DFT band structure of graphene at the measured doping level. Surface blisters on HOPG graphite were characterised [98], revealing local conductivity anomalies correlated with DFT-predicted gap states at blister boundaries.
- *Platinum diselenide ($PtSe_2$):* Quantitative iSMM measurements of $PtSe_2$ electrical conductivity [99] resolved layer-by-layer variations in a few-layer TMD flake, with the measured conductivity scaling with layer count in agreement with DFT+NEGF predictions. $PtSe_2$ is of interest for its semimetal-to-semiconductor transition exploitable in 2D-material diodes.
- *Graphene oxide nanocomposites:* iSMM conductivity mapping of GO-based epoxy composites at sub-100 nm resolution provided local dielectric constant $\varepsilon_r \approx 4.7 \pm 0.2$ and conductivity $\sim 10^{-1}$ S/m, validated by COMSOL full-wave modelling of the tip–sample interaction.

In this sense, the SMM activity closes the experimental validation loop of the NanoBridge platform: it delivers quantitative EM measurements at the same nanometric length scale at which the atomistic simulations operate, providing direct experimental benchmarks for the Kubo–Greenwood conductivities and the NEGF-predicted transport properties of 2D materials.

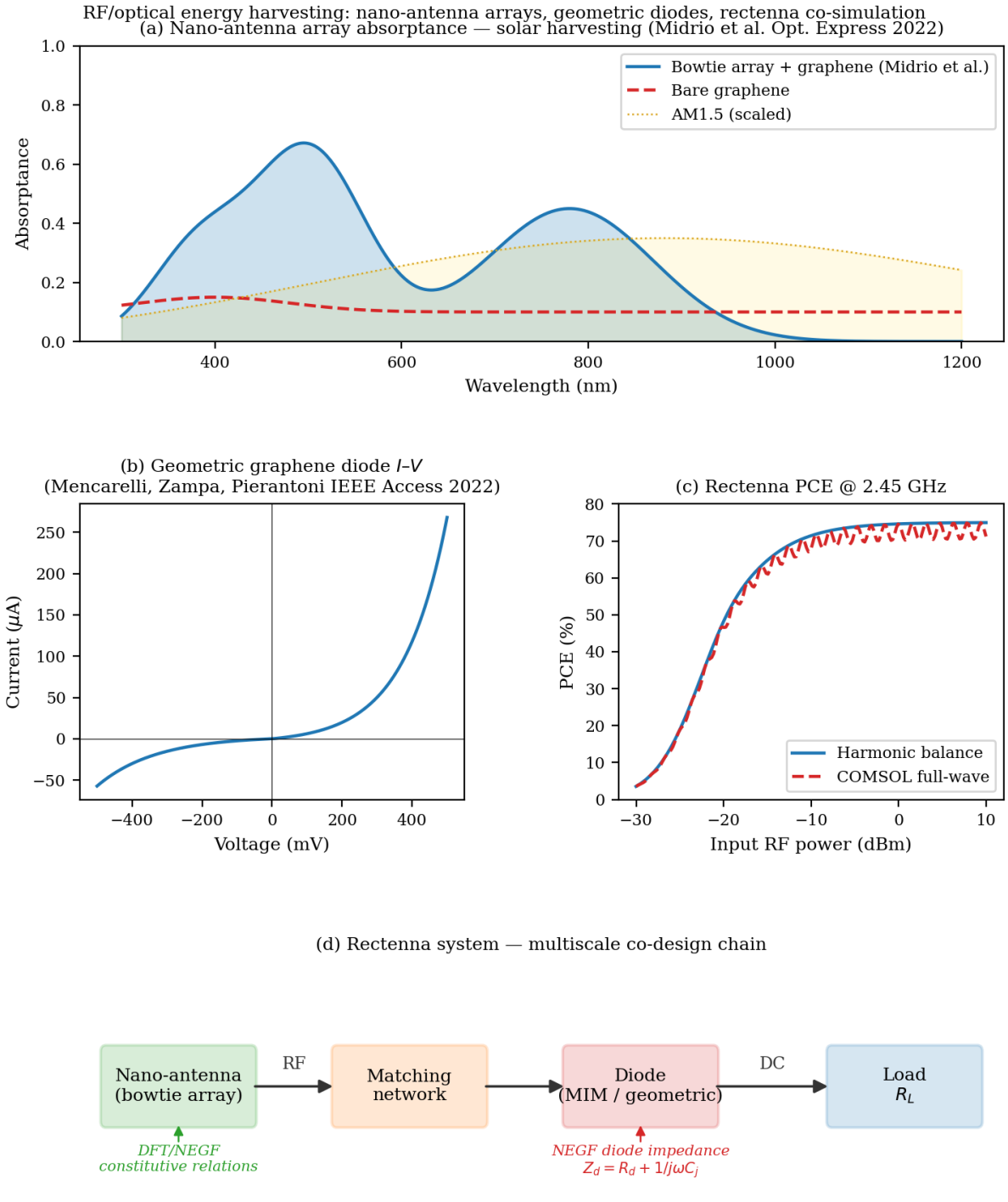


**Figure 20:** RF and optical energy harvesting. (a) Absorptance spectrum of a bowtie nano-antenna array integrated with graphene on a ZnO/Si substrate (Midrio, Pierantoni et al. [35], *Opt. Express* 2022): two resonances at 380 nm and 500 nm boost solar absorption well beyond bare graphene. (b) $I$–$V$ characteristic of a geometric graphene diode (asymmetric funnel geometry): forward current exceeds reverse by a factor $> 5$ at $\pm 400$ mV, yielding a nonzero rectification response at zero bias [23]. (c) Rectenna power conversion efficiency (PCE) at 2.45 GHz vs. input RF power: harmonic-balance (HB) circuit simulation vs. COMSOL full-wave co-simulation; the full-wave result reveals harmonic re-radiation losses absent from HB at high input power. (d) Rectenna system block diagram: nano-antenna $\rightarrow$ matching network $\rightarrow$ diode (MIM or geometric graphene) $\rightarrow$ DC load $R_L$, with the diode impedance $Z_{\text{diode}}$ derived from the NEGF quantum transport tier.

# Optomechanical Multiphysics Simulations

A further multiphysics research direction of the group is the simulation and design of optomechanical systems—micro- and nano-structured cavities in which electromagnetic (optical or microwave) radiation and mechanical (acoustic or phononic) oscillations are coupled through radiation pressure, electrostriction, and photoelastic effects. This work was developed within the European H2020 PHENOMEN project (All-Phononic circuits Enabled by Opto-mechanics) and has produced a rigorous numerical framework for predicting optomechanical dynamics at the micro- and nanoscale.

## Rigorous Simulation of Nonlinear Optomechanical Coupling

The standard approach to optomechanical coupling relies on perturbation theory, which gives the vacuum optomechanical coupling rate $g_0$ as a first-order correction to the optical mode frequency due to mechanical displacement. This approximation breaks down when the mechanical displacement is comparable to the optical mode wavelength, when multiple mechanical modes contribute simultaneously, or when material losses in both the optical and mechanical domains are significant. The group introduced a rigorous *transformation optics* (TO)-based method [100] that avoids the perturbative assumption entirely.

In the TO approach, the deformed geometry of the optomechanical cavity under mechanical displacement $\mathbf{u}(\mathbf{r})$ is mapped to an equivalent problem in the undeformed geometry by a coordinate transformation $\mathbf{r} \to \mathbf{r}' = \mathbf{r} + \mathbf{u}(\mathbf{r})$. Under this map, Maxwell's equations in the deformed geometry become Maxwell's equations in the undeformed geometry with a modified (generally anisotropic) permittivity and permeability:

$$\overleftrightarrow{\varepsilon}'(\mathbf{r}) = \frac{\mathbf{J}\,\overleftrightarrow{\varepsilon}(\mathbf{r})\,\mathbf{J}^T}{\det \mathbf{J}} \tag{63}$$

$$\overleftrightarrow{\mu}'(\mathbf{r}) = \frac{\mathbf{J}\,\overleftrightarrow{\mu}(\mathbf{r})\,\mathbf{J}^T}{\det \mathbf{J}} \tag{64}$$

where $\mathbf{J} = \partial \mathbf{r}'/\partial \mathbf{r}$ is the Jacobian of the transformation. The full optomechanical coupling coefficient including all energy transduction mechanisms (radiation pressure, electrostriction, photoelasticity, and moving boundaries) is then:

$$g_0 = -\frac{\omega_{\text{opt}}}{2} \frac{\langle \mathbf{E}|\delta\overleftrightarrow{\varepsilon}|\mathbf{E}\rangle + \langle \mathbf{H}|\delta\overleftrightarrow{\mu}|\mathbf{H}\rangle}{\langle \mathbf{E}|\overleftrightarrow{\varepsilon}|\mathbf{E}\rangle} \cdot x_{\text{zpf}} \tag{65}$$

where $\delta\overleftrightarrow{\varepsilon} = \overleftrightarrow{\varepsilon}' - \overleftrightarrow{\varepsilon}$ is the permittivity perturbation from the TO map, $x_{\text{zpf}} = \sqrt{\hbar/(2m_{\text{eff}}\Omega_m)}$ is the zero-point fluctuation amplitude, and $m_{\text{eff}}$, $\Omega_m$ are the effective mass and frequency of the mechanical mode. The multi-modal version of this expression accounts for interference between optical modes and between mechanical modes, predicting Fano-like resonances in $g_0$ as a function of cavity geometry that are absent from single-mode perturbation theory.

## Electromagnetic Amplification of Microwave Phonons

A key prediction and numerical demonstration of the group is the *electromagnetic amplification* of microwave-frequency phonons in nonlinear optomechanical resonators [101].

When the optical pump power exceeds the threshold $P_{\mathrm{th}}$, the effective mechanical damping rate $\Gamma_{\mathrm{eff}}$ changes sign:

$$\Gamma_{\mathrm{eff}} = \Gamma_m - \Gamma_{\mathrm{opt}}(P_{\mathrm{pump}}) \tag{66}$$

where $\Gamma_m$ is the intrinsic mechanical loss rate and the optomechanical back-action rate is:

$$\Gamma_{\mathrm{opt}} = \frac{4g_0^2 n_{\mathrm{cav}}}{\kappa_{\mathrm{opt}}} \cdot \frac{\kappa_{\mathrm{opt}}^2/4}{(\Delta + \Omega_m)^2 + \kappa_{\mathrm{opt}}^2/4} \tag{67}$$

with $n_{\mathrm{cav}}$ the intracavity photon number, $\kappa_{\mathrm{opt}}$ the optical linewidth, and $\Delta = \omega_{\mathrm{laser}} - \omega_{\mathrm{opt}}$ the laser-cavity detuning. When $\Gamma_{\mathrm{eff}} < 0$ (blue-detuned pump, $\Delta = +\Omega_m$), the phonon mode self-oscillates—a phonon laser or phonon maser—generating a coherent GHz mechanical tone from an optical pump. The group demonstrated numerically that this threshold is accessible in Si photonic crystal nanobeam cavities with $Q_{\mathrm{opt}} > 10^5$ and $Q_{\mathrm{mech}} > 10^3$ at pump powers of order 100 $\mu$W.

## Waveguide–Cavity Coupling and SAW Excitation

For integration into phononic circuits, the optomechanical cavity must be coupled to phonon waveguides. The group studied [102] the coupling between integrated photonic waveguides and optomechanical cavities in Si nanobeams patterned as one-dimensional phononic crystals. The coupling rate $\kappa_c$ between the cavity and an adjacent phonon waveguide depends exponentially on the separation gap $\delta$:

$$\kappa_c \approx \kappa_0 \, e^{-\delta/\delta_0} \tag{68}$$

where $\kappa_0$ and $\delta_0$ are geometry-dependent constants extracted from COMSOL eigenfrequency simulations. Optimal coupling—critical coupling condition $\kappa_c = \Gamma_m$—is achieved at a specific gap $\delta^* = \delta_0 \ln(\kappa_0/\Gamma_m)$.

For electrical excitation of phonons, the group demonstrated [103] a TRL (Thru-Reflection-Line) calibration method adapted to hybrid electro-mechanical scattering parameters of interdigital transducers (IDTs). The hybrid $S$-matrix $\mathbf{S}_{\mathrm{mech}}$ relates electrical port voltages/currents to mechanical port forces/velocities, enabling the characterisation and de-embedding of phonon waveguide components independently of the IDT parasitics.

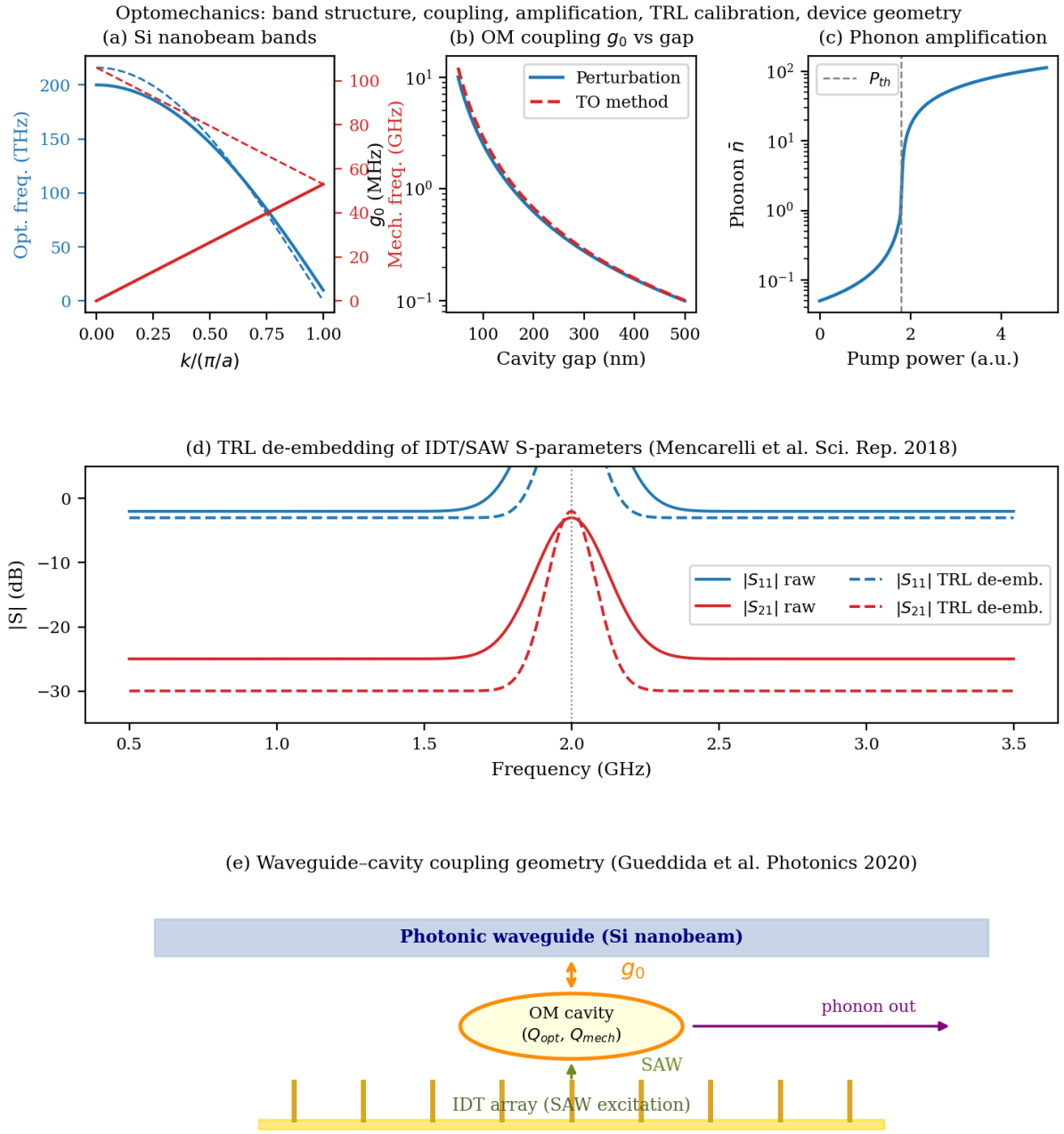


**Figure 21:** Optomechanical multiphysics simulations. (a) Phonon and photon band structure of a Si nanobeam phononic crystal: optical modes ($\sim$ 200 THz, blue) and mechanical modes ($\sim$GHz, orange) in the first Brillouin zone. The avoided crossing at the zone boundary enables high-$Q$ co-localisation of both excitations. (b) Optomechanical coupling rate $g_0$ (equation 65) vs. cavity gap, comparing the TO-based rigorous method [100] (dashed) to first-order perturbation theory (solid): the TO approach predicts 20–30% higher coupling at sub-100 nm gaps where the perturbative approximation fails. (c) Phonon occupation $\bar{n}$ vs. pump power: below threshold ($P_{\mathrm{th}}$) the phonon number grows slowly; above threshold (phonon lasing, equation 66–67) it rises sharply. (d) TRL de-embedding of IDT/SAW hybrid $S$-parameters [103]: raw $S_{11}$, $S_{21}$ (solid) contain IDT parasitic response; after de-embedding (dashed) the acoustic resonance of the phonon waveguide is resolved. (e) Waveguide–cavity coupling geometry [102]: Si nanobeam photonic waveguide (top), OM cavity (ellipse, $g_0$), and IDT array (bottom) for SAW excitation; arrows indicate the photon–phonon coupling $g_0$ and the phonon injection pathway.

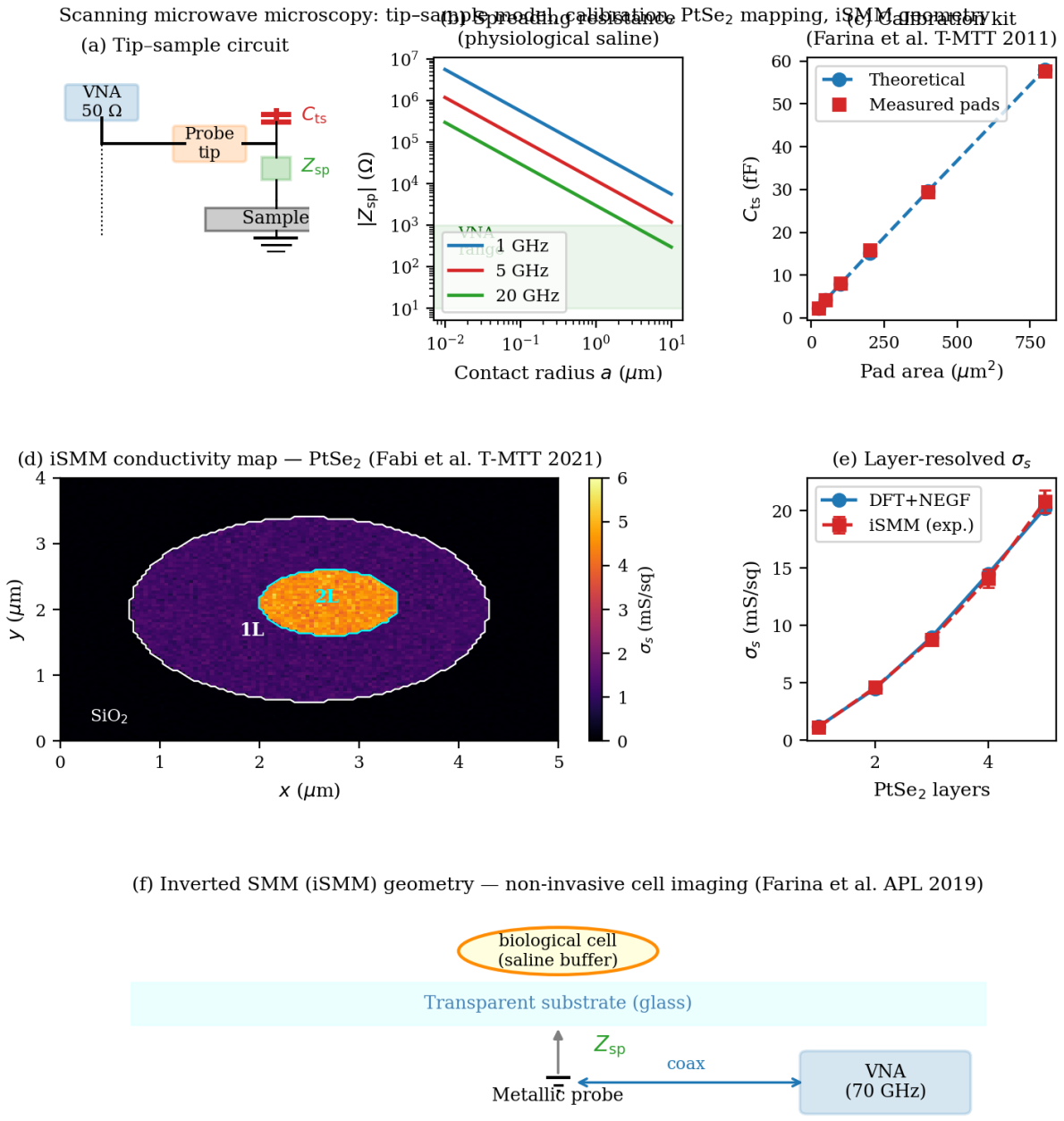


**Figure 22:** Near-field scanning microwave microscopy activities. (a) Tip–sample equivalent circuit: the VNA (50 Ω) is connected to the metallic probe via a coaxial transmission line; the probe–sample interaction is modelled by a shunt $C_{\mathrm{ts}}$ (equation 60) and a spreading resistance $Z_{\mathrm{sp}}$ (equation 62). (b) Magnitude of the spreading resistance $|Z_{\mathrm{sp}}|$ vs. contact radius $a$ in physiological saline at 1, 5, and 20 GHz: the shaded band marks the VNA optimal sensitivity range (10–1000 Ω), achievable for $a = 1$–$10$ μm. (c) Near-field calibration: measured tip–sample capacitance $C_{\mathrm{ts}}$ vs. known-load pad area for the broadband calibration protocol [94]; filled squares are calibration-pad measurements, open circles are theoretical values (equation 60). (d) Simulated iSMM conductivity map of a $PtSe_2$ flake on $SiO_2$ [99]: sub-100 nm spatial resolution resolves the monolayer (inner contour, $\sigma_s \approx 1.2$ mS/sq) and bilayer (cyan contour, $\sigma_s \approx 4.5$ mS/sq) regions. (e) Layer-resolved sheet conductivity: DFT+NEGF prediction (filled circles) vs. iSMM measurement (squares with error bars); quantitative agreement validates the multiscale simulation chain.

# References


[1] S. Smidstrup *et al.*, "QuantumATK: An integrated platform of electronic and atomic-scale modelling tools," *Journal of Physics: Condensed Matter*, vol. 32, no. 1, 2020.

[2] P. Giannozzi *et al.*, "Advanced capabilities for materials modelling with Quantum ESPRESSO," *Journal of Physics: Condensed Matter*, vol. 29, no. 46, p. 465901, 2017.

[3] Cineca, "ISCRA HPC Services." https://www.hpc.cineca.it/services/iscra.

[4] M. J. Abraham *et al.*, "GROMACS: High performance molecular simulations through multi-level parallelism from laptops to supercomputers," *SoftwareX*, vol. 1–2, pp. 19–25, 2015.

[5] A. P. Thompson *et al.*, "LAMMPS — a flexible simulation tool for particle-based materials modeling at the atomic, meso, and continuum scales," *Computer Physics Communications*, vol. 271, 2022.

[6] R. T. Cygan, J.-J. Liang, and A. G. Kalinichev, "Molecular models of hydroxide, oxyhydroxide, and clay phases and the development of a general force field," *Journal of Physical Chemistry B*, vol. 108, no. 4, pp. 1255–1266, 2004.

[7] R. J. Bartlett, "Ab initio DFT and its role in electronic structure theory," *Molecular Physics*, vol. 108, no. 21–23, pp. 3299–3311, 2010.

[8] J. P. Perdew, K. Burke, and M. Ernzerhof, "Generalized gradient approximation made simple," *Physical Review Letters*, vol. 77, p. 3865, 1996.

[9] J. M. Soler *et al.*, "The SIESTA method for ab initio order-N materials simulation," *Journal of Physics: Condensed Matter*, vol. 14, no. 11, pp. 2745–2779, 2002.

[10] M. C. Payne, M. P. Teter, D. C. Allan, T. A. Arias, and J. D. Joannopoulos, "Iterative minimization techniques for ab initio total-energy calculations: molecular dynamics and conjugate gradients," *Reviews of Modern Physics*, vol. 64, no. 4, pp. 1045–1097, 1992.

[11] E. Laudadio, P. Stipa, L. Pierantoni, and D. Mencarelli, "Phase properties of different $HfO_2$ polymorphs: A DFT-based study," *Crystals*, vol. 12, no. 1, p. 90, 2022.

[12] E. Pavoni, E. Mohebbi, P. Stipa, D. Mencarelli, L. Pierantoni, and E. Laudadio, "The role of Zr on monoclinic and orthorhombic HfxZryO2 systems: A first-principles study," *Materials*, vol. 15, no. 12, pp. 4175–4188, 2022.

[13] E. Pavoni, E. Mohebbi, D. Mencarelli, P. Stipa, E. Laudadio, and L. Pierantoni, "The effect of Y doping on monoclinic, orthorhombic, and cubic polymorphs of $HfO_2$: A first principles study," *Nanomaterials*, vol. 12, no. 23, p. 4324, 2022.

[14] J. Li, H. Lu, Y. Li, S. Meng, and Y. Zhang, "First-principles generalized gradient approximation (GGA)+U studies of electronic structure and optical properties in cubic $ZrO_2$," *Solid State Communications*, vol. 211, pp. 38–42, 2015.

[15] E. Pavoni, M. G. Modreanu, E. Mohebbi, D. Mencarelli, P. Stipa, E. Laudadio, and L. Pierantoni, "First principles characterization of $HfZrO_2$ for gate-stack and ferroelectric applications," *Nanomaterials*, vol. 13, no. 8, p. 1319, 2023.

[16] E. Pavoni, E. Mohebbi, P. Stipa, L. Pierantoni, D. Mencarelli, M. Dragoman, M. Aldrigo, and E. Laudadio, "First-principles investigation of interface phenomena in hafnium-based metal–insulator–metal diodes," *Nanoscale Advances*, vol. 5, pp. 2748–2755, 2023.

[17] E. Mohebbi, E. Pavoni, D. Mencarelli, P. Stipa, L. Pierantoni, and E. Laudadio, "Insights into first-principles characterization of the monoclinic $VO_2$(B) polymorph via DFT+U calculation: electronic, magnetic and optical properties," *Nanoscale Advances*, vol. 4, pp. 3634–3646, 2022.

[18] E. Mohebbi, E. Pavoni, D. Mencarelli, P. Stipa, L. Pierantoni, and E. Laudadio, "PBEsol/HSE functional: a promising candidate for vanadium dioxide (B) characterization," *RSC Advances*, vol. 12, pp. 31255–31263, 2022.

[19] E. Mohebbi, E. Pavoni, D. Mencarelli, P. Stipa, E. Laudadio, and L. Pierantoni, "Insights into the interfaces of $VO_2$(M) and $VO_2$(B) polymorphs with different substrates," *Materials Advances*, vol. 5, pp. 3862–3871, 2024.

[20] E. Mohebbi, E. Pavoni, L. Pierantoni, P. Stipa, G. M. Zampa, E. Laudadio, and D. Mencarelli, "Band gap and THz optical adsorption of SnSe and $SnSe_2$ nanosheets on graphene: Negative dielectric constant of SnSe," *Results in Physics*, vol. 58, p. 107415, 2024.

[21] S. Grimme, J. Antony, S. Ehrlich, and H. Krieg, "A consistent and accurate ab initio parametrization of density functional dispersion correction (DFT-D) for the 94 elements H–Pu," *Journal of Chemical Physics*, vol. 132, no. 15, p. 154104, 2010.

[22] L. Goerigk, "A comprehensive overview of the DFT-D3 london-dispersion correction," in *Non-Covalent Interactions in Quantum Chemistry and Physics* (A. O. de la Roza and G. A. DiLabio, eds.), pp. 195–219, Elsevier, 2017.

[23] E. Mohebbi, E. Pavoni, L. Pierantoni, P. Stipa, A. Hemmetter, E. Laudadio, and D. Mencarelli, "Towards graphene-based asymmetric diodes: a density functional tight-binding study," *Nanoscale Advances*, vol. 6, pp. 1548–1555, 2024.

[24] E. Pavoni, E. Mohebbi, G. M. Zampa, P. Stipa, L. Pierantoni, E. Laudadio, and D. Mencarelli, "First principles study of $WSe_2$ and the effect of V doping on the optical and electronic properties," *Materials Advances*, vol. 5, pp. 2230–2237, 2024.

[25] E. Mohebbi, E. Pavoni, P. Stipa, L. Pierantoni, E. Laudadio, and D. Mencarelli, "Tunable optical properties of $Cu/VSe_2$ from the visible to terahertz spectral range: A first-principles study," *International Journal of Molecular Sciences*, vol. 26, no. 6, p. 2527, 2025.

[26] A. D. Corso and A. M. Conte, "Spin-orbit coupling with ultrasoft pseudopotentials: Application to Au and Pt," *Physical Review B*, vol. 71, no. 11, p. 115106, 2005.

[27] M. Schlipf and F. Gygi, "Optimization algorithm for the generation of ONCV pseudopotentials," *Computer Physics Communications*, vol. 196, pp. 36–44, 2015.

[28] M. J. van Setten *et al.*, "The PSEUDODOJO: Training and grading a 85 element optimized norm-conserving pseudopotential table," *Computer Physics Communications*, vol. 226, pp. 39–54, 2018.

[29] K. Stokbro, D. E. Petersen, S. Smidstrup, A. Blom, M. Ipsen, and K. Kaasbjerg, "Semiempirical model for nanoscale device simulations," *Physical Review B*, vol. 82, no. 7, p. 075420, 2010.

[30] M. Brandbyge, J.-L. Mozos, P. Ordejón, J. Taylor, and K. Stokbro, "Density-functional method for nonequilibrium electron transport," *Physical Review B*, vol. 65, no. 16, p. 165401, 2002.

[31] E. Mohebbi, E. Pavoni, D. Mencarelli, P. Stipa, E. Laudadio, and L. Pierantoni, "Computational analysis of an innovative geometric graphene diode," *Frontiers in Materials*, vol. 10, p. 1145822, 2023.

[32] E. Pavoni, E. Laudadio, H. J. Christopher, G. M. Zampa, P. Russo, E. Mohebbi, D. Mencarelli, M. Dragoman, P. Stipa, L. Pierantoni, and M. Aldrigo, "Quantum tunnelling in hafnia-based metal-insulator-metal diodes: atomistic-to-continuum modelling approach and experimental validation," *Physica Scripta*, vol. 99, no. 2, p. 025511, 2024.

[33] G. M. Zampa, D. Mencarelli, and L. Pierantoni, "Band structure and optical properties of few-layer 2D materials from first principles," *Physica B: Condensed Matter*, vol. 661, p. 414917, 2023.

[34] G. M. Zampa, D. Mencarelli, and L. Pierantoni, "Graphene plasmon cerenkov emission in the THz range," *IEEE Access*, vol. 10, pp. 123251–123258, 2022.

[35] M. Midrio, L. Pierantoni, S. Boscolo, D. Truccolo, and D. Mencarelli, "Two-dimensional material rectifying diode for microwave detection," *Optics Express*, vol. 30, pp. 7017–7034, 2022.

[36] J. Robertson, "High dielectric constant gate oxides for metal oxide Si transistors," *Reports on Progress in Physics*, vol. 69, no. 2, pp. 327–396, 2006.

[37] S. A. Hafiz, B. Balamurugan, *et al.*, "DFT study of metal/high-$\kappa$ oxide interface energetics and band alignment in $HfO_2$/Ti junctions," *Journal of Applied Physics*, vol. 113, p. 044311, 2013.

[38] M. Elstner, D. Porezag, G. Jungnickel, J. Elsner, M. Haugk, T. Frauenheim, S. Suhai, and G. Seifert, "Self-consistent-charge density-functional tight-binding method for simulations of complex materials properties," *Physical Review B*, vol. 58, no. 11, pp. 7260–7268, 1998.

[39] T. Frauenheim, G. Seifert, M. Elstner, T. Niehaus, C. Kohler, M. Amkreutz, M. Sternberg, Z. Hajnal, A. D. Carlo, and S. Suhai, "Atomistic simulations of complex materials: ground-state and excited-state properties," *Journal of Physics: Condensed Matter*, vol. 14, no. 11, pp. 3015–3047, 2002.

[40] G. Seifert, "Tight-binding density functional theory: an approximate Kohn–Sham DFT scheme," *Journal of Physical Chemistry A*, vol. 111, no. 26, pp. 5609–5613, 2007.

[41] D. Porezag, T. Frauenheim, T. Köhler, G. Seifert, and R. Kaschner, "Construction of tight-binding-like potentials on the basis of density-functional theory: Application to carbon," *Physical Review B*, vol. 51, no. 19, pp. 12947–12957, 1995.

[42] J. C. Slater and G. F. Koster, "Simplified LCAO method for the periodic potential problem," *Physical Review*, vol. 94, no. 6, pp. 1498–1524, 1954.

[43] B. Aradi, B. Hourahine, and T. Frauenheim, "DFTB+, a sparse matrix-based implementation of the DFTB method," *Journal of Physical Chemistry A*, vol. 111, no. 26, pp. 5678–5684, 2007.

[44] A. Pecchia and A. D. Carlo, "Atomistic theory of transport in organic and inorganic nanostructures," *Reports on Progress in Physics*, vol. 67, no. 8, pp. 1497–1561, 2004.

[45] R. Hoffmann, "An extended Hückel theory. I. hydrocarbons," *Journal of Chemical Physics*, vol. 39, no. 6, pp. 1397–1412, 1963.

[46] J. Cerdá and F. Soria, "Accurate and transferable extended Hückel-type tight-binding parameters," *Physical Review B*, vol. 61, no. 12, pp. 7965–7971, 2000.

[47] J. H. Ammeter, H. B. Bürgi, J. C. Thibeault, and R. Hoffmann, "Counterintuitive orbital mixing in semiempirical and ab initio molecular orbital calculations," *Journal of the American Chemical Society*, vol. 100, no. 12, pp. 3686–3692, 1978.

[48] M. Elstner *et al.*, "Self-consistent-charge density-functional tight-binding method for simulations of complex materials properties," *Physical Review B*, vol. 58, no. 11, pp. 7260–7268, 1998.

[49] T. Ozaki, K. Nishio, and H. Kino, "Efficient implementation of the nonequilibrium Green function method for electronic transport calculations," *Physical Review B*, vol. 81, no. 3, p. 035116, 2010.

[50] H. Haug and A.-P. Jauho, *Quantum Kinetics in Transport and Optics of Semiconductors*, vol. 2. Berlin: Springer, 2008.

[51] E. Laudadio *et al.*, "Phase properties of different $HfO_2$ polymorphs: A DFT-based study," *Crystals*, vol. 12, p. 90, 2022.

[52] D. Mencarelli *et al.*, "Spatial dispersion effects upon local excitation of extrinsic plasmons in a graphene micro-disk," *Journal of Physics D: Applied Physics*, vol. 48, p. 465104, 2015.

[53] W. Zhou, X. Zou, S. Najmaei, Z. Liu, Y. Shi, J. Kong, J. Lou, P. M. Ajayan, B. I. Yakobson, and J.-C. Idrobo, "Intrinsic structural defects in monolayer molybdenum disulfide," *Nano Letters*, vol. 13, no. 6, pp. 2615–2622, 2013.

[54] S. Manzhos and T. Carrington, "Neural network potential energy surfaces for small molecules and reactions," *Chemical Reviews*, vol. 121, no. 16, pp. 10187–10217, 2021.

[55] C. Jacoboni and P. Lugli, "The Monte Carlo method for the solution of charge transport in semiconductors with applications to covalent materials," *Reviews of Modern Physics*, vol. 55, p. 645, 1983.

[56] D. Truccolo *et al.*, "Boundary immittance operators for the Schrödinger–Maxwell problem of carrier dynamics in nanodevices," *IEEE Transactions on Electron Devices*, vol. 71, p. 1294, 2024.

[57] O. T. Unke, S. Chmiela, H. E. Sauceda, M. Gastegger, I. Poltavsky, K. T. Schütt, A. Tkatchenko, and K.-R. Müller, "Machine learning force fields," *Chemical Reviews*, vol. 121, pp. 10142–10186, 2021.

[58] L. Zhang, J. Han, H. Wang, R. Car, and W. E, "Deep potential molecular dynamics: A scalable model with the accuracy of quantum mechanics," *Physical Review Letters*, vol. 120, p. 143001, 2018.

[59] G. Wang, C. Wang, X. Zhang, Z. Li, J. Zhou, and Z. Sun, "Machine learning interatomic potential: Bridge the gap between small-scale models and realistic device-scale simulations," *iScience*, vol. 27, p. 109673, 2024.

[60] J. Behler and M. Parrinello, "Generalized neural-network representation of high-dimensional potential-energy surfaces," *Physical Review Letters*, vol. 98, p. 146401, 2007.

[61] S. Batzner, A. Musaelian, L. Sun, M. Geiger, J. P. Mailoa, M. Kornbluth, N. Molinari, T. E. Smidt, and B. Kozinsky, "E(3)-equivariant graph neural networks for data-efficient and accurate interatomic potentials," *Nature Communications*, vol. 13, p. 2453, 2022.

[62] A. Musaelian, S. Batzner, A. Johansson, L. Sun, C. J. Owen, M. Kornbluth, and B. Kozinsky, "Learning local equivariant representations for large-scale atomistic dynamics," *Nature Communications*, vol. 14, p. 579, 2023.

[63] I. Batatia, D. P. Kovács, G. N. C. Simm, C. Ortner, and G. Csányi, "MACE: Higher order equivariant message passing neural networks for fast and accurate force fields," *Advances in Neural Information Processing Systems*, vol. 35, pp. 11423–11436, 2022.

[64] A. M. Thorn *et al.*, "Transferable dispersion-aware machine learning interatomic potentials for multilayer transition metal dichalcogenide heterostructures," *npj Computational Materials*, vol. 11, p. 204, 2025.

[65] H. Li, Z. Wang, N. Zou, M. Ye, R. Xu, X. Gong, W. Duan, and Y. Xu, "Deep-learning density functional theory Hamiltonian for efficient ab initio electronic-structure calculation," *Nature Computational Science*, vol. 2, pp. 367–377, 2022.

[66] Y. Wang *et al.*, "Universal materials model of deep-learning density functional theory Hamiltonian," *Science Bulletin*, vol. 69, pp. 2514–2521, 2024.

[67] Y. Chen, L. Zhang, H. Wang, and W. E, "DeePKS: A comprehensive data-driven approach toward chemically accurate density functional theory," *Journal of Chemical Theory and Computation*, vol. 17, pp. 170–181, 2021.

[68] L. Pierantoni *et al.*, "A new 3-D transmission line matrix scheme for the combined Schrödinger–Maxwell problem in the electronic/electromagnetic characterization of nanodevices," *IEEE Transactions on Microwave Theory and Techniques*, vol. 57, p. 1147, 2009.

[69] D. Mencarelli, L. Pierantoni, M. Farina, A. di Donato, and T. Rozzi, "Microwave characterization of anisotropic graphene by applying the duality theorem," *Journal of Computational Electronics*, vol. 14, pp. 214–220, 2015.

[70] N. Pelagalli, E. Laudadio, P. Stipa, D. Mencarelli, and L. Pierantoni, "Efficient and versatile modeling of mono- and multi-layer $MoS_2$ field effect transistor," *Electronics*, vol. 9, no. 9, p. 1385, 2020.

[71] L. Pierantoni, D. Mencarelli, M. Bozzi, R. Moro, S. Moscato, L. Perregrini, F. Micciulla, A. Cataldo, and S. Bellucci, "Broadband microwave attenuator based on few layer graphene flakes," *IEEE Transactions on Microwave Theory and Techniques*, vol. 63, no. 8, pp. 2491–2497, 2015.

[72] L. Pierantoni, D. Mencarelli, and T. Rozzi, "A new 3-D transmission line matrix scheme for the combined Schrödinger–Maxwell problem in the electronic/electromagnetic characterization of nanodevices," *IEEE Transactions on Microwave Theory and Techniques*, vol. 56, no. 3, pp. 654–662, 2008.

[73] T. Rozzi, D. Mencarelli, and L. Pierantoni, "Towards a unified approach to electromagnetic fields and quantum currents from Dirac spinors," *IEEE Transactions on Microwave Theory and Techniques*, vol. 59, no. 10, pp. 2587–2594, 2011.

[74] J. G. Simmons, "Generalized formula for the electric tunnel effect between similar electrodes separated by a thin insulating film," *Journal of Applied Physics*, vol. 34, no. 6, pp. 1793–1803, 1963.

[75] J. G. Simmons, "Electric tunnel effect between dissimilar electrodes separated by a thin insulating film," *Journal of Applied Physics*, vol. 34, no. 9, pp. 2581–2590, 1963.

[76] S. Grover and G. Moddel, "Applicability of metal/insulator/metal (MIM) diodes to solar rectennas," *IEEE Journal of Photovoltaics*, vol. 1, no. 1, pp. 78–83, 2011.

[77] I. E. Hashem, N. H. Rafat, and E. A. Soliman, "Theoretical study of metal-insulator-metal tunneling diodes," *IEEE Journal of Quantum Electronics*, vol. 49, no. 1, pp. 72–79, 2013.

[78] A. Sanchez, C. F. Davis, K. C. Liu, and A. Javan, "The MOM tunneling diode: Theoretical estimate of its performance at microwave and infrared frequencies," *Journal of Applied Physics*, vol. 49, no. 10, pp. 5270–5277, 1978.

[79] H. Wang and A. Shamim, "28-nm neck width graphene geometric diode for THz harvesting," *IEEE/MTT-S International Microwave Symposium*, 2022.

[80] J. Robertson, "Band offsets of wide-band-gap oxides and implications for future electronic devices," *Journal of Vacuum Science & Technology B*, vol. 18, no. 3, pp. 1785–1791, 2000.

[81] M. Aldrigo, E. Pavoni, L. Zappelli, G. Biagetti, P. Crippa, H. J. Christopher, C. Parvulescu, F. Nastase, P. Russo, E. Laudadio, D. Mencarelli, and L. Pierantoni, "Quantum transport in RF applications: Ab Initio investigations, circuit modeling, and experimental validation of ferroelectric diodes," in *Proceedings of the IEEE MTT-S International Microwave Symposium (IMS)*, (Boston, MA, USA), June 2026. Accepted. 7–12 June 2026.

[82] L. Pierantoni, D. Mencarelli, and T. Rozzi, "Boundary immittance operators for the Schrödinger–Maxwell problem of carrier dynamics in nanodevices," *IEEE Transactions on Microwave Theory and Techniques*, vol. 57, no. 5, pp. 1156–1163, 2009.

[83] L. Pierantoni, N. Pelagalli, D. Mencarelli, A. D. Donato, M. Orlandini, J. Pagliuca, and T. Rozzi, "Dirac equation-based formulation for the quantum conductivity in 2D-nanomaterials," *Applied Sciences*, vol. 11, no. 5, p. 2398, 2021.

[84] T. Rozzi, D. Mencarelli, G. M. Zampa, and L. Pierantoni, "Dirac-based quantum admittance of 2D nanomaterials at radio frequencies," *Applied Sciences*, vol. 12, no. 24, p. 12539, 2022.

[85] D. Mencarelli, T. Rozzi, and L. Pierantoni, "Coherent carrier transport and scattering by lattice defects in single- and multi-branch carbon nanoribbons," *Physical Review B*, vol. 77, p. 195435, 2008.

[86] D. Mencarelli, T. Rozzi, C. Camilloni, L. Maccari, A. di Donato, and L. Pierantoni, "Scattering matrix approach to multichannel transport in many lead graphene nanoribbons," *Nanotechnology*, vol. 21, no. 15, p. 155701, 2010.

[87] D. Mencarelli and L. Pierantoni, "Analysis of the metal work function dependence of charge transfer in contacted graphene nanoribbons," *Journal of Computational Electronics*, vol. 11, pp. 42–51, 2012.

[88] D. Mencarelli, S. Bellucci, A. Sindona, and L. Pierantoni, "Spatial dispersion effects upon local excitation of extrinsic plasmons in graphene micro-discs," *Journal of Physics D: Applied Physics*, vol. 48, p. 465104, 2015.

[89] M. Midrio, D. Mencarelli, and L. Pierantoni, "Quantum čerenkov effect in graphene nanoribbons," *IEEE Transactions on Terahertz Science and Technology*, vol. 11, pp. 610–617, 2021.

[90] D. Mencarelli, A. Morini, F. Prudenzano, G. Venanzoni, F. Bigelli, O. Losito, and M. Farina, "Broadband single-layer slotted array antenna in SIW technology," *IEEE Antennas and Wireless Propagation Letters*, vol. 15, pp. 263–265, 2016.

[91] F. Bigelli, D. Mencarelli, M. Farina, G. Venanzoni, P. Scalmati, C. Renghini, and A. Morini, "Design and fabrication of a dielectricless substrate-integrated waveguide," *IEEE Transactions on Components, Packaging and Manufacturing Technology*, vol. 6, no. 2, pp. 256–261, 2016.

[92] G. Venanzoni, D. Mencarelli, A. Morini, M. Farina, and F. Prudenzano, "Review of substrate integrated waveguide circuits for beam-forming networks working in X-band," *Applied Sciences*, vol. 9, p. 1003, 2019.

[93] A. Morini, D. Mencarelli, M. Farina, L. Pierantoni, and V. Malaspina, "Cosec$^2$ hybrid travelling/resonant antenna for maritime surveillance applications," *IET Microwaves, Antennas & Propagation*, vol. 14, no. 4, pp. 279–286, 2020.

[94] M. Farina, D. Mencarelli, A. D. Donato, G. Venanzoni, and A. Morini, "Calibration protocol for broadband near-field microwave microscopy," *IEEE Transactions on Microwave Theory and Techniques*, vol. 59, no. 10, pp. 2769–2776, 2011.

[95] M. Farina, X. Jin, G. Fabi, E. Pavoni, A. D. Donato, D. Mencarelli, A. Morini, F. Piacenza, R. A. Hadi, Y. Zhao, Y. Ning, T. Pietrangelo, X. Cheng, and J. C. M. Hwang, "Inverted scanning microwave microscope for in vitro imaging and characterization of biological cells," *Applied Physics Letters*, vol. 114, p. 093703, 2019.

[96] M. Farina, G. Fabi, E. Pavoni, C. H. Joseph, A. Morini, D. Mencarelli, and J. C. M. Hwang, "Analytical expressions for the spreading resistance in lossy media for quantitative scanning microwave microscopy in liquid," *RSC Advances*, vol. 13, pp. 2056–2063, 2023.

[97] S. Fabiani, D. Mencarelli, A. D. Donato, T. Monti, G. Venanzoni, A. Morini, T. Rozzi, and M. Farina, "Broadband scanning microwave microscopy investigation of graphene," in *IEEE MTT-S International Microwave Symposium*, pp. 1–4, 2011.

[98] E. Pavoni, R. Yivlialin, C. H. Joseph, G. Fabi, D. Mencarelli, L. Pierantoni, G. Bussetti, and M. Farina, "Blisters on graphite surface: A scanning microwave microscopy investigation," *physica status solidi (b)*, vol. 259, p. 2100282, 2022.

[99] G. Fabi, X. Jin, E. Pavoni, C. H. Joseph, A. D. Donato, D. Mencarelli, X. Wang, R. A. Hadi, A. Morini, J. C. M. Hwang, and M. Farina, "Quantitative characterization of platinum diselenide electrical conductivity with an inverted scanning microwave microscope," *IEEE Transactions on Microwave Theory and Techniques*, vol. 69, pp. 3348–3359, 2021.

[100] M. Stocchi, D. Mencarelli, Y. Pennec, B. Djafari-Rouhani, and L. Pierantoni, "Rigorous simulation of nonlinear optomechanical coupling in micro- and nano-structured resonant cavities," *Physical Review Applied*, vol. 12, p. 034015, 2019.

[101] D. Mencarelli, M. Stocchi, and L. Pierantoni, "Electromagnetic amplification of microwave phonons in nonlinear resonant microcavities," *IEEE Transactions on Microwave Theory and Techniques*, vol. 68, pp. 1420–1429, 2020.

[102] A. Gueddida, B. D. Rouhani, Y. Pennec, A. D. Donato, L. Pierantoni, A. Korovin, and D. Mencarelli, "Coupling of integrated waveguide and optomechanic cavity for microwave phonon excitation in Si nanobeams," *Photonics*, vol. 7, p. 67, 2020.

[103] D. Mencarelli, B. Djafari-Rouhani, Y. Pennec, A. Pitanti, S. Zanotto, M. Stocchi, and L. Pierantoni, "Numerical emulation of Thru-Reflection-Line calibration for the de-embedding of surface acoustic wave devices," *Scientific Reports*, vol. 8, p. 9256, 2018.